Title: Dopamine D1 receptor expression in dlPFC inhibitory parvalbumin neurons may contribute to higher visuospatial distractibility in marmosets versus macaques

Authors: Joyce MKP[*1], Ivanov TG[*2], Krienen FM[3,4], Mitchell JF[5], Ma S[1,17], Inoue W[6,7], Nandy AS[1,8,9], Datta D[10], Duque A[1], Arellano J[1], Gupta R[2], Gonzalez-Burgos G[11], Lewis DA[11,12], Sestan N[1,8,12,13], McCarroll SA[4,14], Martinez-Trujillo J[6,7,15,16], Froudist-Walsh S[2+], Arnsten AFT[1,8,9+]

Affiliations:
*-co-first authorship/equal contributions
+corresponding authors
1-Department of Neuroscience, Yale University School of Medicine, New Haven, CT 06510, USA
2-School of Engineering, Mathematics & Technology, University of Bristol, Bristol, UK
3-Princeton Neuroscience Institute, Princeton University, Princeton, NJ 08544, USA
4-Department of Genetics, Harvard Medical School, Boston, MA 02115, USA
5-Department of Brain and Cognitive Sciences, University of Rochester, New York, NY 14627, USA
6-Robarts Research Institute, Western University, London ON N6A 5K8, Canada
7-Department of Physiology and Pharmacology, Schulich School of Medicine and Dentistry, University of Western Ontario, London, ON N6A 5C1, Canada
8-Wu Tsai Institute, Yale University, New Haven, CT 06510, USA
9-Kavli Institute for Neuroscience, Yale University School of Medicine, New Haven, CT 06510, USA
10-Department of Psychiatry, Yale University School of Medicine, New Haven, CT 06510, USA
11-Department of Psychiatry, University of Pittsburgh, Pittsburgh, PA 15260, USA
12-Department of Neuroscience, University of Pittsburgh, Pittsburgh, PA 15213, USA
13-Department of Genetics and Comparative Medicine, Program in Cellular Neuroscience, Neurodegeneration and Repair, and Yale Child Study Center, Yale University School of Medicine, New Haven CT 06510, USA
14-Stanley Center for Psychiatric Research, Broad Institute of MIT and Harvard, Cambridge, MA 02142, USA
15-Department of Psychiatry, Schulich School of Medicine and Dentistry, University of Western Ontario, London, ON N6A 5C1, Canada
16-Western Institute for Neuroscience, University of Western Ontario, London, ON N6A 3K7, Canada
17-Institute of Neuroscience, CAS Center for Excellence in Brain Science and Intelligence Technology, University of Chinese Academy of Sciences, Chinese Academy of Sciences, Shanghai 200031, China

Corresponding authors:
Dr. Amy F.T. Arnsten, Albert E. Kent Professor of Neuroscience
Dept. Neuroscience, Yale Medical School
333 Cedar St., New Haven, CT USA 06510
Email: amy.arnsten@yale.edu
Phone: 203-785-4431 Mobile: 203-530-3954 FAX: 203-785-5263

Dr. Seán Froudist-Walsh
School of Engineering, Mathematics & Technology, University of Bristol
BS8 1UB, Bristol, UK
Email: sean.froudist-walsh@bristol.ac.uk
Phone: +447541515541

Acknowledgements:
This research was funded by NSF 2015276 to AFTA, JMT, FMK and SAM, as well as by a Bristol Neuroscience of Mental Health award (co-funded by Steve Scobie and Anne Graham) and BBSRC BB/X013243/1 to SFW. We thank the Yale Center for Cellular & Molecular Imaging Confocal Facility for usage of their Zeiss LSM 880 Airyscan microscope. The modeling work was carried out using the high-performance computing facilities of the Advanced Computing Research Centre, University of Bristol – http://www.bristol.ac.uk/acrc/. We are grateful to Kristy Gibbs, Lisa Ciavarella, Tracy Sadlon, Sam Johnson, and Michelle Wilson for their technical expertise. Additionally, we thank Albert Compte, Joao Barbosa, Paul Anastasiades, John Hongyu Meng, and Christos Constantinidis for helpful discussions, as well as Matt Jones, Ulysse Klatzmann, Aswathi Thrivikraman, Dabal Pedamonti, and Eva Sevenster for feedback on the manuscript. Further thanks to Benjamin Corrigan and Diego Buitrago-Piza for their behavioral task illustrations, which we have adapted for Figure 1.

Abstract:
Marmosets and macaques are common non-human primate models of cognition, but evidence suggests that marmosets perform more poorly and appear more distractible during cognitive tasks. The dorsolateral prefrontal cortex (dlPFC) plays a key role in regulating attention, and prior research in macaques suggests that dopaminergic modulation and inhibitory parvalbumin (PV) neurons could contribute to distractibility during cognitive performance. Thus, we compared the two species using a visual fixation task with distractors, performed molecular and anatomical analyses of dlPFC, and linked functional microcircuitry with cognitive performance using computational modeling. We found that marmosets are more distractible than macaques, and that marmoset dlPFC PV neurons contain higher levels of dopamine-1 receptor (D1R) transcripts, similar to mice, and higher levels of D1R protein. The computational model suggested that higher D1R expression in marmoset dlPFC PV neurons may increase distractibility by suppressing dlPFC microcircuits, e.g., when dopamine is released in dlPFC to salient stimuli.

Declaration of Interests: The authors have nothing to declare.

Author Contributions: AFTA, MKPJ, TGI, and SFW designed the study; MKPJ collected and analyzed anatomical data; TGI, RG, and SFW designed and performed the modeling; FM and SAM collected and analyzed transcriptomics data; GGB and DAL provided macaque brain tissue for transcriptomics performed by FM; SM and NS collected and analyzed phylogenetic transcriptomics dataset; JFM and ASN performed and analyzed the behavioral testing; IW and JMT provided the marmoset tissue for immunofluorescence; MKPJ, TGI, SFW, and AFTA wrote the first draft and all authors revised and edited subsequent drafts of the article.

Word count: 4928
Figures: 5

Introduction

Marmosets are an increasingly attractive non-human primate model due to their small size, ease of handling, short breeding cycle, brief lifespan, and amenability to emerging genetic and molecular technologies (e.g.,[1]). The use of marmosets has already proven successful in modeling many psychiatric and mental processes[2-4]. Yet the extent of their translational validity and similarity to macaques in cognitive domains is still under investigation, as very few studies have directly compared the two species in the same tasks. One early study[5] found that marmosets required more trials to match macaque performance on a delayed-response working memory task, and marmoset performance, compared to that of macaques, worsened more with longer delays. Additionally, marmosets invariably failed the task if they became distracted away from the screen, while macaques could overcome external distractions and respond correctly[5]. More recently, assays of attentional regulation show that macaques[6] have a superior ability to regulate attention shifting compared to marmosets[7]. These data are consistent with anecdotal reports that high levels of distractibility in marmosets can interfere with training[8]. Although a more comprehensive comparison of cognitive abilities across these species remains necessary, the evidence suggests that marmosets perform more poorly in tasks with higher cognitive demands, and that they may be more susceptible than macaques to distractibility, which we define as behavioral or neurophysiological responses to external task-irrelevant stimuli. These cross-species differences in cognitive function necessitate a comparison of the neural circuitry supporting these processes in marmosets and macaques.

Core cognitive processes, such as working memory and attention, may rely on partially overlapping neuronal populations in the dlPFC[9, 10], although some have argued for more dissociation[11]. Studies of macaque dlPFC have revealed that extensive recurrent excitation among the pyramidal neurons in specialized microcircuits of deep layer III maintains persistent firing activity across a working memory delay period, even in the presence of distractors[12, 13]. These layer III pyramidal neurons, known as Delay cells, are considered essential for maintaining mental representations in the absence of external stimuli. Inhibitory, GABAergic PV neurons have also been central to early theories of the cellular basis of attention and working memory[12-14], though their exact contributions to cognitive function and particularly distractibility are still unclear. Evidence suggests that fast-spiking, putative PV neurons may be actively recruited during the delay period to sculpt the spatial tuning of excitatory Delay cell population activity[12, 15, 16], and adequate spatial tuning is critical for distractor resistance. Putative fast-spiking, PV neurons likely provide feedback inhibition onto the same pyramidal neurons that excite them[17-25]. They may also provide feedforward lateral inhibition onto pyramidal neurons with different spatial tuning[17-25], which could include pyramidal neurons with preferred directions that are either near to or far from the preferred direction of the pyramidal neurons that excite the putative PV neuron. Whether the microcircuit components contributing to working memory in macaque dlPFC are present in marmoset dlPFC remains largely unknown. Marmosets have a smaller dlPFC than macaques[26-28], and marmoset prefrontal pyramidal neurons have fewer spines on the basal dendrites[29], which could be necessary for the recurrent excitation that supports persistent activity. Nevertheless, dlPFC delay-related persistent activity was recently verified in marmosets[30], suggesting that they have key microcircuit components to support working memory.

Neuromodulators such as dopamine (DA) have powerful effects on dlPFC function in macaques[31] and marmosets[32]. DA is released in the dlPFC to salient stimuli, whether they are rewarding or aversive[33]. In macaques, DA largely influences dlPFC function via D1Rs[31, 34], with an inverted-U dose-response, where mid-range levels of D1R stimulation facilitate working memory[35, 36], while higher levels impair working memory[37, 38]. In macaque dlPFC, D1Rs predominate on the dendritic spines of layer III pyramidal

neurons[34, 36, 39], but they are also found on the dendrites of PV neurons[40]. *Ex vivo* physiological studies in rodents[41] and macaques[42] have shown that D1R stimulation increases the intrinsic excitability of fast-spiking, putative PV neurons, which could affect their roles in the structured inhibition and spatial tuning of excitatory Delay cells *in vivo*. A recent study using iontophoresis and electrophysiology in macaque dlPFC showed that DA, via D1Rs, modulates fast-spiking, likely PV, neurons during delay periods with distractor challenges[43]. Given the D1R-mediated increase in the excitability of fast-spiking, putative PV neurons, we hypothesized that higher D1R expression levels in layer III dlPFC PV neurons in marmosets, compared to macaques, may significantly degrade distractor resistance if there is excessive inhibition of pyramidal neuron firing. Because these layer III microcircuits are altered in schizophrenia[44], stage III/IV Alzheimer's disease[45], and stress and mood disorders[46], understanding their common and divergent properties across primates is critical when modeling neural mechanisms of cognitive disorders.

Here, we first compared the ability of marmosets and macaques to maintain gaze on a central point in the presence of visual distractors. Next, we assessed D1R expression in layer III dlPFC PV neurons across the two species by mining and integrating data from existing single nucleus RNA sequencing (snRNA-seq) datasets, including data from mouse and human, and performing detailed immunohistochemistry. Finally, we incorporated the anatomical measurements of D1R expression into a visuospatial working memory model to simulate the effect of higher D1R expression on inhibitory fast-spiking, putative PV neurons in a layer III dlPFC microcircuit. Our results demonstrate that marmosets exhibit more distractibility than macaques, even in a basic visual fixation task, and that marmosets have higher D1R expression in layer III dlPFC PV neurons. Lastly, our modeling shows that higher D1R expression in fast-spiking, putative PV neurons in a layer III dlPFC microcircuit may contribute to higher marmoset distractibility by causing task-related persistent activity to be suppressed even at moderate levels of DA release, e.g. in response to a salient environmental stimulus, making them more susceptible to interference by distractors. Our results suggest fundamental species differences in the effect of DA on dlPFC microcircuits and offer insights into mechanisms of distractibility in working memory.

Results

Marmosets are more distractible than macaques in a basic visual fixation task

To quantify differences in distractibility between marmosets and macaques, we used a basic fixation task with minimal cognitive demands, only requiring sustained attention. Specifically, we examined the ability of subjects to hold visual fixation on a central point while distracting stimuli flashed in the visual periphery. This task is commonly used with rhesus macaques to map receptive field properties of neurons in visual cortical areas[47], and marmosets can perform it with a reasonable degree of success[48]. We analyzed data previously collected from marmosets and macaques performing this task under comparable visual stimulation conditions[47, 48]. Animals were required to maintain fixation within a 1-2° radius around the fixation point while high contrast Gabor stimuli flashed at random positions in the periphery at 60 Hz. Monkeys were rewarded with a drop of juice for holding fixation at increasingly longer periods up to a maximum of 3 seconds.

The macaques could ignore the distractors for over twice as long as any of the marmosets (Figure 1), holding fixation for a median duration of 2.57 seconds as compared to 1.05 seconds in marmosets, which was a significant cross-species difference (Ranksum test, $p=0.044$). Although individual marmoset performance varied considerably, no single marmoset achieved performance equivalent to either of the macaques (individuals shown with black circles, Figure 1). These data suggest that even when the cross-

species comparison task has minimal cognitive demands, a fundamental difference in distractibility exists between the species.

Marmosets have higher DRD1 expression in dlPFC PVALB neurons than macaques

Analyses from independent snRNA-seq datasets revealed that *DRD1* (the gene encoding D1R) expression in *PVALB* (the gene encoding PV) neuron clusters of the marmoset dlPFC is markedly higher than in macaque dlPFC (Figure 2). First, we compared *DRD1* expression in *PVALB* neuron clusters of young adult marmosets[49] and macaques[50], and found higher expression of *DRD1* in *PVALB* clusters from marmoset compared to macaque (Figure 2A). Less than 1% of macaque *PVALB* nuclei were *DRD1*+, while about 20% of the marmoset *PVALB* nuclei were *DRD1*+. Then, our second dataset[51, 52] corroborated and extended these findings, demonstrating that *DRD1* expression in *PVALB* clusters of marmosets exceeded expression in macaques, and that marmoset dlPFC and mouse frontal cortex exhibit high *DRD1* expression in *PVALB* clusters, (Figure 2B), whereas human dlPFC had the lowest expression. Overall, these results suggest an inverse relationship between *DRD1* expression and phylogenetic position among the species studied here.

Marmoset layer III dlPFC PV neurons have higher D1R expression than macaques

To examine the *in situ* expression of D1R protein in layer III dlPFC, we labeled D1R and PV using immunohistochemistry (Figure 3A-B). In both species, D1R labeling was observed in the cytoplasmic and nuclear regions of PV neurons and putative pyramidal neurons, consistent with previous findings[40, 53, 54]. Labeling was also observed in pyramidal neuron apical dendrites, confirmed by co-labeling with the cytoskeletal protein microtubule-associated protein 2 (MAP2, Figure S1). In our double-labeled PV/D1R tissue, we sampled from layer III in both species using confocal microscopy. The sampled images were analyzed in two independent ways: (1) using an automated higher throughput colocalization analysis of PV neuronal segments (Figure 3C-D), which computed the spatial extent to which PV+ processes contain colocalized PV+/D1R+ pixels; and (2) then using a manual analysis of D1R fluorescence intensity signal in PV somata (Figure 3G-H), to determine the proportion of neurons that were negative for D1R or expressed D1R weakly, moderately, or strongly.

For the colocalization analysis, we first used automatic segmentation to isolate PV neuronal processes. We then computed an index of colocalization, called the Manders' Overlap Coefficient (MOC), to determine the proportion of each PV segment that contained colocalized D1R+/PV+ pixels. Marmoset PV segments had a higher degree of colocalization with D1R than macaque PV segments (Figure 3C). For both species, segmented particles found in the PV neuron soma and proximal dendrites had a higher degree of D1R colocalization than those in non-proximal dendrites (Figure 3D), and this disparity was greater in marmosets. The second analysis (schematized in Figure S2) binned PV neurons according to their level of D1R expression, and showed that macaques had slightly more D1R-negative PV neurons than marmosets (Figure 3E-H), which was directionally similar to the species difference in the proportions of *DRD1*+ *PVALB* nuclei found in our sn-RNAseq data. The trend continued with marmosets having more D1R-strong PV neurons than macaques (Figure 3H), though this was not significant.

Computational modeling of the effect of the species difference in D1R expression in layer III dlPFC PV neurons on distractibility

Given that D1R stimulation increases the intrinsic excitability of fast-spiking, putative PV neurons in macaque layer III dlPFC, and that PV neurons shape the spatial tuning of excitatory Delay cell population activity, we investigated whether higher D1R expression in marmoset layer III dlPFC PV neurons may contribute to higher visuospatial distractibility. Specifically, we predict that identical fractions of active D1R receptors on PV neurons between species would cause consistently higher microcircuit inhibition in marmosets, thus suppressing task-related persistent activity within the typical, mid D1R stimulation range and increasing its susceptibility to interference by distractors. For this purpose, we redesigned a well-established spiking network model[55] of a visuospatial working memory microcircuit in macaque layer III dlPFC (Figure 4A1), which allows the linking of functional microanatomy with cognitive performance. Specifically, in addition to near feature-tuned, regular-spiking excitatory (E) Delay cells (Figure 4A2), we incorporated two new types of fast-spiking inhibitory Delay cells – I_{NEAR} and I_{OPP} – with near-feature and opposite-feature tuning (Figure 4A3-4A4), to replace the unstructured inhibition in the original model, because evidence suggests that putative fast-spiking, PV neurons might instead mediate such structured inhibitory motifs in primary sensory[19-22, 25] and higher order association[17, 18, 23, 24] cortex. Reportedly, I_{NEAR}-mediated inhibition primarily stabilizes the amplitude of the spatially tuned population activity of excitatory Delay cells[56, 57], increasing its robustness to excitatory perturbations[58], like noise. In our visuospatial working memory model, such robustness could thus translate into resistance to distractors, specifically near the target because I_{NEAR}-mediated inhibition is strongest at and around the target position. Conversely, I_{OPP}-mediated inhibition critically enables the competition between opposite feature-tuned Delay cell populations[57, 59, 60]. Accordingly, in our model, I_{OPP}-mediated inhibition may confer higher resistance to far distractors by more strongly suppressing E cells tuned to opposite (vs. near) positions following target presentation, compared to baseline. This increases the stimulus strength necessary to form persistent activity at the farthest positions and disrupt the target-specific persistent activity. Notably, since attentional processes share neuronal substrates with working memory[9, 10], the neurons supporting distractor resistance in our model should partly overlap with those involved in our visual fixation task. Thus, our simulations may identify a plausible neural mechanism for our behavioral measures of visuospatial distractibility.

D1R expression in E and I_{NEAR} cells facilitates the inverted-U response

We considered three cell type-specific D1R expression patterns, and explored which could reproduce the inverted-U relationship between D1R stimulation and persistent firing activity observed experimentally in delayed-response working memory tasks[34, 35, 37] (Figure 4B). Specifically, we built three networks in which E cells always expressed D1Rs, while D1R expression in the inhibitory cells differed. D1Rs were expressed in Network 1 by I_{NEAR} cells; in Network 2 by I_{OPP} cells; and in Network 3, by both I_{NEAR} and I_{OPP} cells. We considered D1R stimulation in terms of D1R occupancy, the fraction of DA-bound D1Rs. We defined five D1R occupancy levels – no (0), low (0.25), mid (0.50), high (0.75) and very high (1) – on a normalized scale ranging from 0 to 1, and evaluated network performance in a visuospatial working memory task. During task trials, we briefly applied a target stimulus at 0° and, later, a distractor stimulus at 180°, the most representationally dissimilar position. We varied the strength of stimuli to identify what strength evoked the most robust inverted-U response. Too weak stimuli will never elicit persistent activity, while too strong stimuli will always cause distractibility. To reproduce the distinct persistent activity regimes of the inverted-U for the macaque, we implemented a set of D1R modulations of synaptic and cellular parameters (details in Methods). Briefly, from no to low D1R occupancy, we increased the NMDAR conductance at E→E synapses[61, 62] ($G_{E\rightarrow E,\ NMDA}$) to facilitate a transition from a transient to a persistent activity regime and (2) decreased AMPAR conductances at E→E and E→I synapses[61, 63] ($G_{E\rightarrow E,\ AMPA}$, $G_{E\rightarrow I,\ AMPA}$) to dampen noise inputs to excitatory and inhibitory cells (Figure 4C1). We also

decreased the firing thresholds of D1R+ inhibitory cells to increase their intrinsic excitability and respectively sculpt, suppress, and silence persistent activity at mid, high, and very high D1R occupancy (Figure 4C2).

Network 1 reproduces the inverted-U over a range of stimulus strengths between ~0.15-0.30 pA with high reliability (max. fraction of complete inverted-Us of 99.1% at 0.20 pA) (Figure S4). Specifically, no and very high D1R occupancies result in transient activations in response to the stimuli due to, respectively, insufficient recurrent excitation and overinhibition (Figure 5A1 and 5E1). Low D1R occupancy elicits an overexcitable, erroneous regime, prone to spatially diffuse and noise-evoked persistent activity at non-stimulus positions (Figure 5B1). Mid D1R facilitates a spatially precise, noise- and distractor-resistant persistent activity regime, suggesting the network represents the memory more accurately during the delay period due to optimal inhibition (Figure 5C1). Notably, high D1R occupancy induces a distractible regime where persistent activity forms around the target position during the delay period but then jumps to the position of the distractor when it appears (Figure 5D1). In contrast, Network 2 cannot reproduce the inverted-U (Figure S4), particularly the distractible persistent activity expected at high D1R occupancy. Network 3 reproduces the inverted-U, like Network 1, but over a narrower range between ~0.20-0.30 pA, and less reliably (max. fraction of complete inverted-Us of 67.7% at 0.25 pA) (Figure S4). Overall, microcircuits featuring D1R+ E and I_{NEAR} cells (Network 1 or 3) appear sufficient to reproduce the inverted-U relationship between D1R stimulation and *in vivo* delay-period neuronal firing activity in visuospatial working memory tasks, unlike a microcircuit featuring only D1R+ E and I_{OPP} cells (Network 2). Our data suggest that D1R+ I_{NEAR} cells may represent D1R+ PV neurons because specifically D1R+ I_{NEAR} cells contributed, alongside D1R+ E cells, to the inverted-U response by increasing their intrinsic excitability with D1R stimulation, which may occur only for D1R+ fast-spiking, putative PV neurons[42]. This corroborates indications[64-66] that PV neurons provide near-feature inhibition in microcircuits.

Most plausible working memory performance in microcircuit with D1R+ I_{NEAR} and E cells, and D1R- I_{OPP} cells

To further evaluate the effect of inhibitory cell-type-specific D1R expression on the visuospatial working memory performance of Networks 1-3 (Figure S5), we simulated the effects of distractors applied at different positions. We focused on Networks 1 and 3, specifically at the typical, mid D1R occupancy level, because Network 2 cannot reproduce the inverted-U for distractors even at 180°. Whereas Network 3 performed poorly due to overwhelming distractibility or errors across distractor positions, with distractor resistance predominating only around 180°, Network 1 was overwhelmingly distractor-resistant at intermediate-to-far positions (112.5°-180°) but also significantly at near positions (45°). We also examined two alternative networks featuring E cells and only, respectively, I_{NEAR} or I_{OPP} cells (all D1R+) (Figure S6). The I_{NEAR}-only network exhibited significant resistance to near distractors (45°) but also overwhelming distractibility and errors across distractor positions. Conversely, the I_{OPP}-only network could overwhelmingly resist far distractors (112.5°-180°), while being highly distractible for near distractors (45°-90°). Furthermore, expectedly, the I_{OPP}-only network could not be distracted by far stimuli at high D1R occupancy (135°-180°). Overall, I_{NEAR} and I_{OPP} cells enable near and far distractor resistance, respectively, and both are necessary for effective microcircuit operations, with D1R expression in only E and I_{NEAR} cells (Network 1) enabling the most plausible performance. These results match experimental observations in a similar visuospatial working memory task[67], which suggested that macaque dlPFC microcircuitry provides some resistance to near distractors (45°) and strong resistance to far distractors (135°, 180°).

Distractibility induced at the typical, mid D1R occupancy level in marmoset

To examine how the higher D1R expression in layer III PV neurons from marmoset dlPFC could affect distractibility in marmosets, we integrated our anatomical findings into the most functionally plausible Network 1. Specifically, given the cross-species difference in D1R expression in PV neurons (Figure 3), and since D1R+ I_{NEAR} cells likely represent D1R+ PV neurons, we assumed that more D1Rs will be DA-bound on I_{NEAR} cells in marmoset compared to macaque, provided there is similar extracellular DA concentration in dlPFC across conditions between both species. Essentially, the same D1R occupancy signifies greater D1R stimulation of marmoset dlPFC PV neurons. Thus, we shifted the midpoint of the I_{NEAR} threshold sigmoid from the reference value of 0.50 for the macaque, on the normalized D1R occupancy scale, to 0.36 for the marmoset, based on the difference (0.14) in mean MOCs between the species (Figure 4C2).

As in the macaque, the marmoset shows only transient activity for no and very high D1R occupancy (Figure 5A2 and 5E2). For low D1R occupancy, the marmoset overwhelmingly exhibits erroneous spatially diffuse, noise-driven persistent activity (Figure 5B2), but with a lower frequency of 85.4% compared to the macaque's 97.3% (Figure S7A-S7B). Crucially, for mid D1R occupancy (Figure 5C2), the marmoset demonstrates distractible persistent activity, which can be verified experimentally, with a frequency of 87.2%, unlike the macaque's 99.7% distractor-resistant persistent activity (Figure S7A-S7B). Finally, at high D1R occupancy, the marmoset already transitions to the transient activity regime (Figure 5D2), which occurs at a higher D1R occupancy in the macaque (Figure S7A-S7B). Overall, the model predicts that the higher D1R expression in I_{NEAR} cells (putative D1R+ PV neurons) in marmoset layer III dlPFC shifts the apex and decreasing phase of the inverted-U to lower D1R occupancy levels for the marmoset, compared to the macaque, since the optimal I_{NEAR}-mediated inhibition is closer to the peak NMDAR-mediated excitation. Thus, the typical, mid D1R occupancy range supports spatially precise, noise- and distractor-resistant persistent activity in macaques, while inducing distractible persistent activity in marmosets.

However, because differences in MOC-measured D1R expression may not correspond directly to differences in D1R stimulation, we examined larger sigmoid midpoint shifts (Figure S7C-S7D). Notably, a shift of 0.375 was approximately the largest that still supports (distractible) persistent activity at the typical, mid D1R occupancy in the marmoset before the microcircuit enters a transient activity regime. Thus, shifts between ~0.14-0.375 would capture the cross-species differences in distractibility, while allowing for plausible microcircuit functioning in the typical, mid D1R stimulation range.

Discussion:

We have shown that marmosets are more distractible than macaques, even in a basic visual fixation task. Furthermore, we found that marmosets have higher *DRD1* expression in *PVALB* neurons than macaques, similar to levels in mice, with lowest levels in humans. We then confirmed *in situ* that PV neurons in marmoset layer III dlPFC exhibit higher D1R expression. Finally, our microcircuit model suggests that higher D1R expression in fast-spiking, putative PV neurons (as we observed in marmosets) shifts the distractible persistent activity regime of the inverted-U response leftward, such that the typical, mid levels of D1R occupancy that optimize excitatory Delay cell firing in macaques would suppress dlPFC microcircuits and cause more distractible behavior in marmosets. To our knowledge, this is the first study to examine how D1R expression differences in PV neurons may affect a cognitively engaged, non-human primate dlPFC microcircuit.

Longstanding electrophysiological and behavioral evidence in marmosets and macaques has implicated DA in working memory and distractor resistance[31, 32, 68-70], but specific microcircuit mechanisms remain an active research area. D1R prevalence on the dendritic spines of dlPFC pyramidal neurons positions them to enhance NMDAR actions in the synapse and, thus, strengthen recurrent excitation to facilitate distractor-resistant persistent activity in Delay cell networks[34, 67, 71]. D1Rs may further ensure appropriate tuning of persistent activity by shunting noisy or task-irrelevant network inputs via the opening of K+ channels on spines[34, 38, 72], which affects distractor resistance. Additionally, D1R stimulation may also affect distractor resistance by modulating cortical inhibition. Several microcircuit models of association cortex have already incorporated I_{NEAR}-like[73-76], and also I_{OPP}-like[24, 56, 57, 59], inhibition to account for the growing evidence for these structured inhibitory motifs[16-18, 22-24], thus succeeding early attempts that featured only unstructured[55, 77-81] inhibition. However, despite the long history of simulating D1R effects on dlPFC-mediated cognition[62, 82-88], to our knowledge, no study has investigated how D1R modulation of structured inhibition affects higher cognitive functions. In rodents and macaques, D1Rs have been shown to increase inhibition through fast-spiking[41, 42], non-fast spiking[89], or vasoactive intestinal peptide-expressing (VIP) inhibitory neurons[90]. Here, we simulated D1R modulation of inhibition strictly based on evidence in macaque layer III dlPFC that D1Rs excite fast-spiking, putative PV neurons[42]. Specifically, we differentiated fast-spiking I_{NEAR} and I_{OPP} cells in a classic visuospatial working memory microcircuit model, and explored how three inhibitory cell-type-specific D1R expression profiles impact working memory function. We found that a microcircuit that features excitatory and both inhibitory Delay cell types and where D1Rs modulate E cells and I_{NEAR} cells (putative D1R+ PV neurons) can reproduce the inverted-U relationship between D1R stimulation and persistent activity observed in macaques *in vivo*[37], and also capture the distractor distance-dependent pattern of working memory performance measured behaviorally in macaques[67]. Hence, optimal D1R stimulation may principally facilitate stabilization of the amplitude of the spatially tuned population activity of excitatory Delay cells[14, 57, 58], and thus also possibly near distractor resistance.

On the other hand, the competition between opposite feature-tuned excitatory Delay cell populations, and thus far distractor resistance, may be independent of D1R modulation because microcircuits featuring D1R+ I_{OPP} cells, which increase their excitability with D1R stimulation, seem functionally implausible. In particular, our Network 2 (and the I_{OPP}-only network) could not reproduce the distractible regime of the inverted-U for distractors at 180°, likely because when D1R stimulation increases the strength of I_{OPP}-mediated inhibition enough to disrupt target-specific persistent activity, at far distractor positions the I_{OPP}–mediated inhibition becomes even stronger, precluding distractor-specific persistent activity from forming. Also, Network 3 exhibited overwhelming distractibility across distractor positions at mid D1R occupancy in the macaque, possibly due to overinhibition caused by twice as many I cells increasing their excitability, compared to Network 1. However, due to the combinatorial explosion of possibilities, we did not explore other more intricate inhibitory cell-type-specific D1R expression patterns, microcircuit configurations, etc., which could allow D1Rs to modulate competition between excitatory Delay cell populations while preserving plausible microcircuit function. Thus, while the role of D1Rs in the stabilization of persistent activity is reasonably supported by our modeling findings, evidence about D1R involvement in competitive dynamics is inconclusive.

By integrating our anatomical results into our most functionally plausible microcircuit configuration (Network 1), we propose that differential D1R modulation of layer III dlPFC PV neurons may underlie some cognitive differences between marmosets and macaques. Specifically, the higher D1R expression in layer III dlPFC PV neurons in marmosets may contribute to their higher distractibility by shifting the

distractible persistent activity regime of the inverted-U response to the typical, mid D1R occupancy range. Conversely, the same level of DA stimulation in macaques supports appropriately tuned and distractor-resistant persistent activity for visuospatial working memory performance. Interestingly, the D1R occupancy range that induces erroneous persistent activity in the increasing phase of the inverted-U contracted for the marmoset in our modeling, predicting that this species is less susceptible to internal distractions (context-irrelevant mental representations, formed without sensory input, that overtake network dynamics). Notably, however, the model assumes extracellular DA concentration in dlPFC is similar across physiological or environmental conditions between the species, and hence mid D1R occupancy is the level at which they both function normally. To our knowledge, no studies have demonstrated species differences in DA innervation of dlPFC. However, DA release could vary significantly over time for marmosets and macaques, and thus both species may utilize the entire D1R occupancy scale more frequently, instead of primarily functioning within the mid D1R occupancy range. In that scenario, a reduced range of D1R occupancies that support distractor-resistant persistent activity in marmosets (e.g., Figure S7C) could better explain their higher distractibility. Otherwise, the fewer spines on the basal dendrites of pyramidal neurons, potentially leading to weaker recurrent excitation, in marmoset dlPFC[29] could also significantly contribute to the higher distractibility. In our model, decreasing the maximum strength of E→E synapses for the marmoset would account for this species difference. In effect, this would cap recurrent excitation to a lower level, and the D1R-mediated increase of $G_{\mathrm{E\rightarrow E,\ NMDA}}$ would not facilitate the same amplitude of persistent activity as in the macaque, thus decreasing the distractor resistance of the microcircuit.

Importantly, a recent model suggested that D1R modulation of somatostatin (SST; similar to calbindin (CB) in primates) and VIP (similar to calretinin (CR) in primates) inhibitory neurons also affects working memory performance[88]. The I_{OPP} cells in our study may represent D1R-/PV+ neurons, perhaps about a third of the total layer III dlPFC PV population according to our manual anatomical analysis (Figure 3H). Alternately, SST/CB neurons have been implicated in opposite feature-tuned inhibition[24, 60, 88, 91] and can display fast spikes[92-94], like PV neurons and the inhibitory cells in our model. Since CB neurons target the distal dendritic trees of pyramidal neurons[95], theoretical studies[88, 91] have suggested they could dampen inputs into the distal dendrites and thus attenuate the effect of noise or distracting stimuli on network dynamics. However, the identities of distal dendrite inputs are unclear and likely not all task-irrelevant. Moreover, both I_{NEAR} and I_{OPP} cells in our model synapse on the E-cell soma because our E cells lack dendritic compartments, questioning a clear correspondence between I_{OPP} cells and SST/CB neurons, and supporting a correspondence with PV neurons, which target the perisomatic region. Finally, our model lacks disinhibitory VIP/CR neurons, which perform permissive gating for pertinent incoming signals[91, 95-97]. The CR neuron population has expanded in primates[98], and CR neurons are more prominent in the dlPFC compared to earlier parts of the dorsal stream[92], suggesting their prominent role in higher cognition. Future studies should explore species differences in D1R modulation of CB and CR neurons, which are also critical components of cortical microcircuits.

The current findings suggest that DA may have a larger inhibitory effect on dlPFC circuits in marmosets than macaques in response to environmental stimuli. The DA neurons that project to the PFC respond to salient stimuli, whether they are aversive or rewarding[33, 99], and the current data suggest that moderate levels of DA release to a salient stimulus may enhance dlPFC function in a macaque, but be sufficient to activate PV neurons and inhibit dlPFC function in a marmoset, increasing their distractibility. The higher susceptibility of cognitive processes to interference by external stimuli may benefit survival in smaller prey species like marmosets by lowering the threshold for predator detection and instinctive responding. This mechanism may be shared in mice, another small prey species. At higher levels of DA release during

states of uncontrollable stress[100, 101], dlPFC dysfunction is also seen in macaques[38, 101] and humans[102], and may contribute to symptoms of mental illness, e.g., in schizophrenia[103].

To conclude, our multi-scale study explored behavioral correlates of cognitive function, *DRD1* mRNA and D1R protein levels *in situ*, and computational modeling of molecular, cellular, and microcircuit bases of working memory performance. Our findings indicate a general mechanism by which subtle cell type-specific molecular differences in dlPFC microcircuits may significantly affect cognitive function. Specifically, we found that a difference in the expression of one receptor in one cell type, namely D1R in layer III dlPFC PV neurons, may contribute to species differences in distractibility, even in a basic sustained attention task. Notably, we empirically confirm marmosets are more distractible than macaques – a crucial step in understanding the translational validity and viability of the former as non-human primate models of cognition. Furthermore, our results suggest that natural variation in D1R expression in PV neurons in humans may contribute to variation in distractibility.

Figure 1

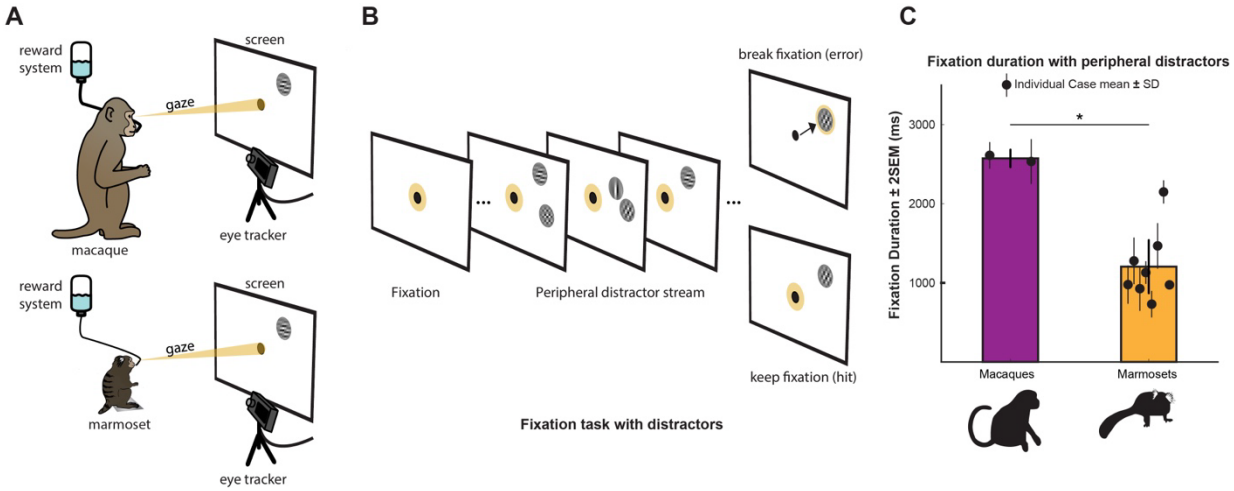

Figure 1 – Macaques held central fixation in the presence of peripheral distractors more than twice as long as marmosets. ***A,*** Schematic of the task setup. A macaque (top) and a marmoset (bottom) face a screen, and an eye tracker monitors their eye movements. Monkeys receive a juice reward for maintaining fixation at the central point in the presence of peripheral distractors. ***B,*** Schematic of the task progression. A point appears at the center of the screen, and the monkey fixes its gaze (yellow) on the central point. Gabor stimuli flash in and out of the periphery, and the monkey is rewarded for maintaining its fixation on the central target ("hit") despite the distracting peripheral stimuli. ***C,*** Time held fixating at a central point in the presence of visual distractors across species. Bars indicate group mean fixation duration for two macaques (purple) and for eight marmosets (orange). Thick black lines depict ± 2 standard error of the mean (SEM); Black circles and thin lines depict individual subject mean fixation duration ± standard deviation (SD). *, $p < 0.05$, Ranksum test.

Figure 2

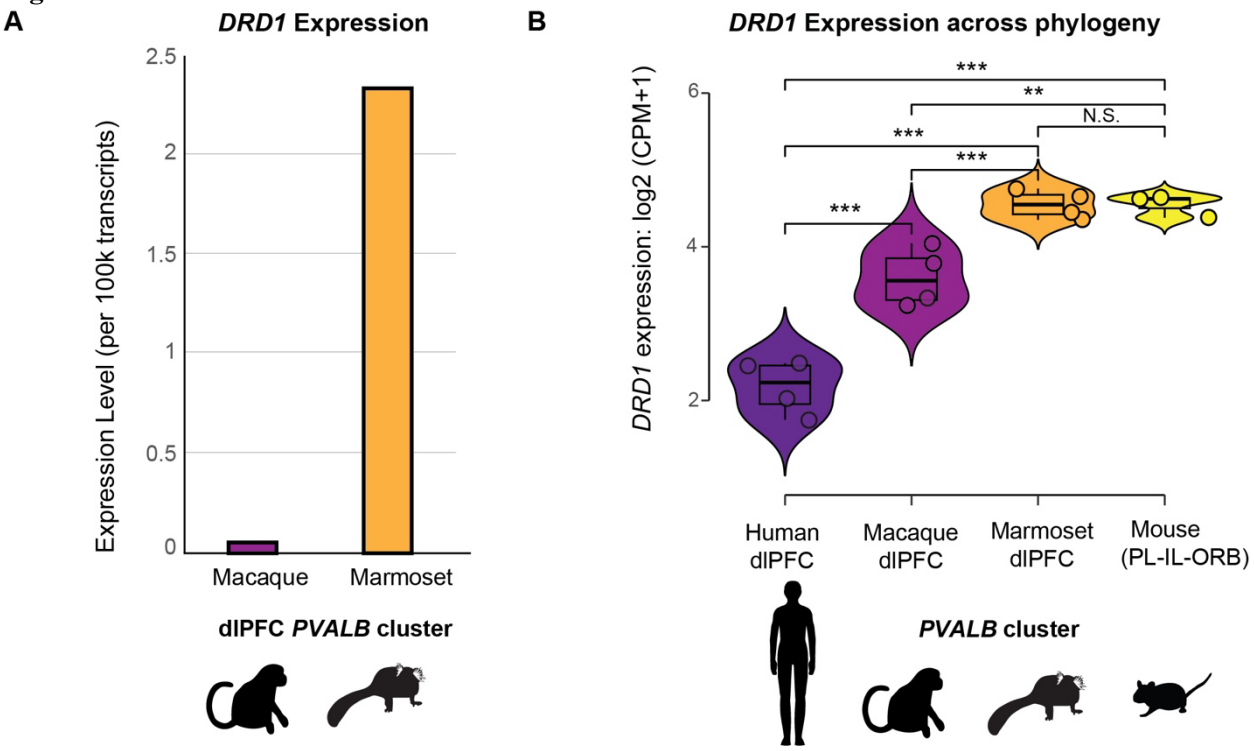

Figure 2 – Marmoset dlPFC *PVALB* neurons have higher *DRD1* expression than macaque *PVALB* neurons. *A,* *DRD1* expression in *PVALB* clusters of the dlPFC in macaques[50] (purple) and marmosets[49] (orange), depicted as expression per 100,000 transcripts. ***B,*** Library size-normalized expression of *DRD1* in adult cortical *PVALB* neurons across human dlPFC (dark purple), macaque dlPFC (plum), marmoset dlPFC (orange), and mouse frontal cortex (yellow). Data mined from Ma *et al.*[52] and Yao *et al.*[51]. Due to the lack of dlPFC homology in mice, we included mouse PL-IL-ORB (prelimbic, infralimbic and orbital regions, yellow) regions,which are analogous substrates for some primate dlPFC cognitive functions. Each dot represents a pseudobulk donor and the significance of the gene expression differences was tested by edgeR[104]. CPM, counts per million; ***, $P < 0.001$; **, $P < 0.01$; N.S., not significant.

1 **Figure 3**

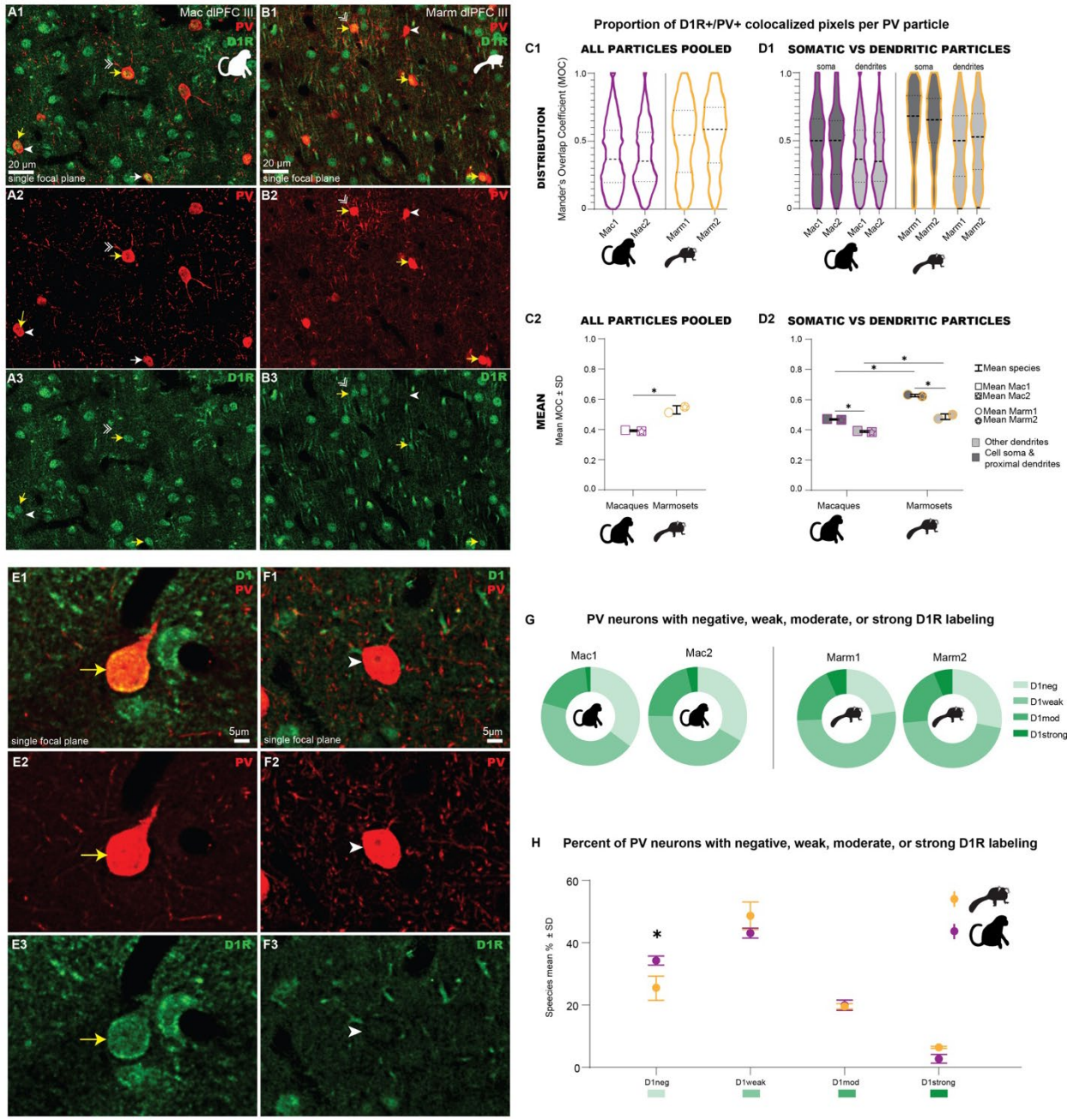
A1
Mac dlPFC III
PV
D1R
20 µm
single focal plane
B1
Marm dlPFC III
A2
B2
A3
B3
E1
D1
PV
F1
5µm
E2
F2
E3
F3
Proportion of D1R+/PV+ colocalized pixels per PV particle
C1
ALL PARTICLES POOLED
D1
SOMATIC VS DENDRITIC PARTICLES
DISTRIBUTION
Mander's Overlap Coefficient (MOC)
soma
dendrites
Mac1
Mac2
Marm1
Marm2
C2
ALL PARTICLES POOLED
D2
SOMATIC VS DENDRITIC PARTICLES
MEAN
Mean MOC ± SD
Macaques
Marmosets
Mean species
Mean Mac1
Mean Mac2
Mean Marm1
Mean Marm2
Other dendrites
Cell soma & proximal dendrites
G
PV neurons with negative, weak, moderate, or strong D1R labeling
D1neg
D1weak
D1mod
D1strong
H
Percent of PV neurons with negative, weak, moderate, or strong D1R labeling
Speecies mean % ± SD

2

Figure 3 – Marmosets have higher correlates of D1R protein expression in layer III dlPFC PV neurons than macaques. ***A-B,*** Confocal photomicrographs with brightness and contrast adjustments depicting a single focal plane imaged in layer III of the macaque **(A)** and marmoset **(B)** dlPFC labeled for PV (red) and D1R (green)**.** Images depict some PV neurons robustly expressing D1R (yellow arrows), or not expressing D1R (white arrowhead). Double-headed white arrow heads depict proximal PV dendrites, defined by being traceable to a parent PV soma. ***C1,*** Violin plots with medians and quartiles, depicting kernel density of the MOC pooled across all PV particles by subject. MOC roughly measures the proportion of D1R+/PV+ pixels in each PV particle. Macaques, purple; marmosets, orange. ***C2,*** Species MOC means for all PV particles (marmosets MOC 0.53±0.03, macaque 0.39±0.01; two-tailed t-test, t(2)=7.283, p=0.0183). ***D1,*** Violin plots with medians and quartiles, depicting kernel density of the MOC across subjects for PV particles segregated into two categories: somata + proximal dendrites, dark grey; or other dendrites not traceable to a soma, light grey. ***D2,*** MOC means across species and proximity to soma classification (mean MOC marmosets soma and proximal, 0.62±0.01; marmoset other 0.47±0.02; macaque soma and proximal 0.47±0.004, macaque other 0.39±0.01; two-way ANOVA, species two-way ANOVA; $F_{1,4}$ = 293.7, p<0.0001; proximity to soma $F_{1,4}$ = 216.9, p=0.0001; interaction $F_{1,4}$ = 16.27, p=0.0157; Pairwise testing with Sidak's multiple comparisons corrections confirmed significant effects within species [marm prox vs. marm other p=0.0011; macaque prox vs. macaque other, p=0.0098], and between species [marm prox vs. macaque prox, p=0.0007; marm other vs. macaque other, p=0.0045]). ***E-F,*** Confocal photomicrographs of single focal planes imaged in layer III dlPFC labeled for PV (red) and D1R (green). Images depict exemplar PV neurons that fell in the D1R strong category (yellow arrows, E), or D1R negative category (white arrowheads, **F**) for analyses in ***G-H***. ***G,*** Proportion of PV neurons falling into four D1R expression bins by subject. Bins were determined objectively for each individual image by binning the image's own D1R signal intensity range. To be classified as D1neg, D1R mean grey value (MGV) in the PV neuron was less than the average D1R MGV sampled in the immunonegative "neuropil". To be classified as D1strong, the D1R MGV of the PV neuron was above the minimum MGV of the most "strongly" labeled D1R neurons in the image, which were typically pyramidal in morphology. Intermediate categories D1weak and D1moderate are intermediate bins between D1neg and D1strong. ***H,*** Species mean for each D1R expression category (mean D1neg marmosets 25±4%, macaques 35±1%, two-way ANOVA, F (3.8) = 215.4, p<0.001, with Sidak's pairwise multiple comparison test, p=0.0221; mean D1neg marmosets 6±0.3%, macaques 3±1%, n.s.). Macaques, purple; marmosets, orange. *, p <0.05 using two-way ANOVA with Sidak's post-hoc pairwise comparisons; D1R, dopamine 1 receptor; dlPFC, dorsolateral prefrontal cortex; Mac, macaque; Marm, marmoset; MOC, Manders' Colocalization Coefficient; PV, parvalbumin; SD, standard deviation.

1 **Figure 4**

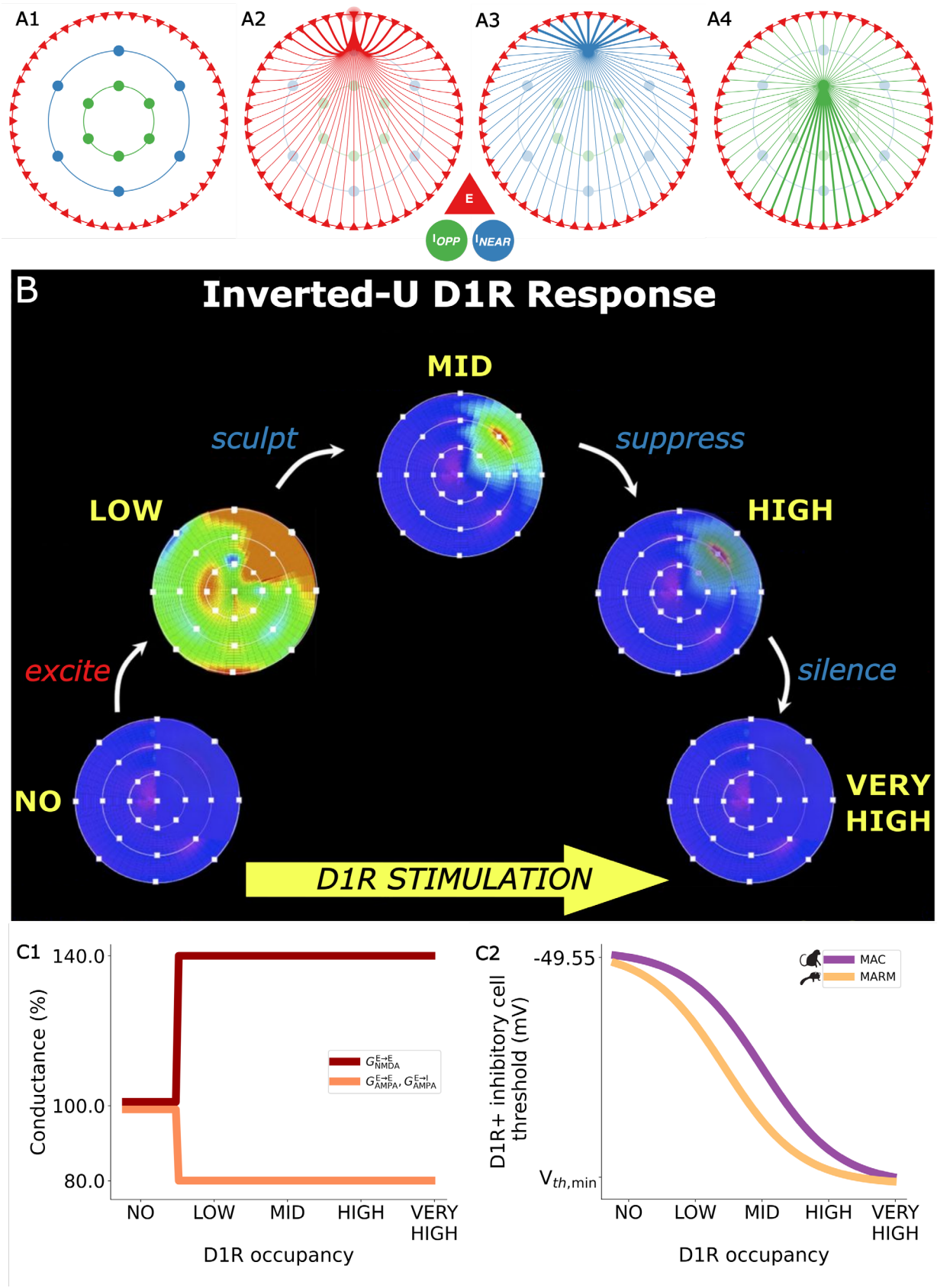
A1
A2
A3
A4
E
I OPP
I NEAR
B
Inverted-U D1R Response
MID
sculpt
suppress
LOW
HIGH
excite
silence
NO
VERY HIGH
D1R STIMULATION
C1
140.0
100.0
80.0
Conductance (%)
NO
LOW
MID
HIGH
VERY HIGH
D1R occupancy
C2
-49.55
D1R+ inhibitory cell threshold (mV)
MAC
MARM
NO
LOW
MID
HIGH
VERY HIGH
D1R occupancy

Figure 4 – Spiking neural network architecture and synaptic connectivity, the inverted-U relationship between D1R stimulation and persistent activity during the delay period of visuospatial working memory tasks, and microcircuit effects of D1R occupancy. ***A***, Simplified schematic representations of **(A1)** the ring architecture of the network comprising 80% near feature-tuned E cells, 10% I_{NEAR} cells, and 10% I_{OPP} cells, with example connectivity profiles for **(A2)** an E cell to each other E cell, **(A3)** an I_{NEAR} cell to all E cells, and **(A4)** an I_{OPP} cell to all E cells, where the source cell is positioned at 0°. For each profile, a halo surrounds the cell from which the projections originate. Projection thickness indicates relative connection strength. E cells are arranged uniformly on a ring, in feature space, according to the angle of the visual stimuli for which they fire the most. Inhibitory cells are also arranged uniformly, based on the angular position of the E cells from which they receive the strongest excitation. The microcircuit features E→E, E→I, I→E, and I→I synapses. E cells send their strongest glutamatergic projections to all cells at the same angle as themselves. I_{NEAR} cells send their strongest GABAergic projections to all cells also at the same angle as themselves, while I_{OPP} cells – to all cells positioned 180° away from them on the ring. ***B,*** Diagram illustrating the idealized inverted-U response, characterized by the delay-period activity during visuospatial working memory tasks in macaques under varying D1R stimulation conditions (adapted with permission from Arnsten *et al.*[34]). At one extreme, no D1R stimulation means E cells cannot sustain persistent activity during the delay period, with only transient activity recorded during stimulus application. In the increasing phase of the inverted-U, low (suboptimal) D1R stimulation induces erroneous (noise-evoked and/or spatially diffuse) persistent activity due to overexcitation. At the peak of the inverted-U, mid (optimal) D1R stimulation sculpts spatially precise, noise- and distractor-resistant persistent activity. Crucially, at the decreasing phase of the inverted-U, high (supraoptimal) D1R stimulation suppresses E cells, decreasing their firing rates, and thus increasing the susceptibility of the persistent activity for target stimuli to disruptions by distractors. Finally, at the other extreme of the inverted-U, very high D1R stimulation silences E cells completely, precluding the formation of persistent activity, again with only transient activity being recorded during stimulus application. ***C1,*** Step-like relationships between D1R occupancy and (1) $G_{E\rightarrow E,\ NMDA}$ and (2) $G_{E\rightarrow E,\ AMPA}$ and $G_{E\rightarrow I,\ AMPA}$, as percentages of their respective baseline values. From no to low D1R occupancy, specifically at $x = 0.125$, we increased $G_{E\rightarrow E,\ NMDA}$ by 40% and decreased $G_{E\rightarrow E,\ AMPA}$ and $G_{E\rightarrow I,\ AMPA}$ by 20%. We applied the same D1R modulations of $G_{E\rightarrow E,\ NMDA}$, $G_{E\rightarrow E,\ AMPA}$, and $G_{E\rightarrow I,\ AMPA}$, in the marmoset and the macaque. ***C2,*** Sigmoidal relationship between D1R occupancy and the species-specific firing thresholds of the D1R+ inhibitory cells across networks. We decreased the firing thresholds of D1R+ inhibitory cells from their baseline ($V_{th,\ base}$) of -49.55 mV at no D1R occupancy, through the low, mid, and high levels, and to a minimum ($V_{th,\ min}$) at the very high level. $V_{th,\ min}$ differed across networks, as listed in Table 4 in Methods.

Figure 5

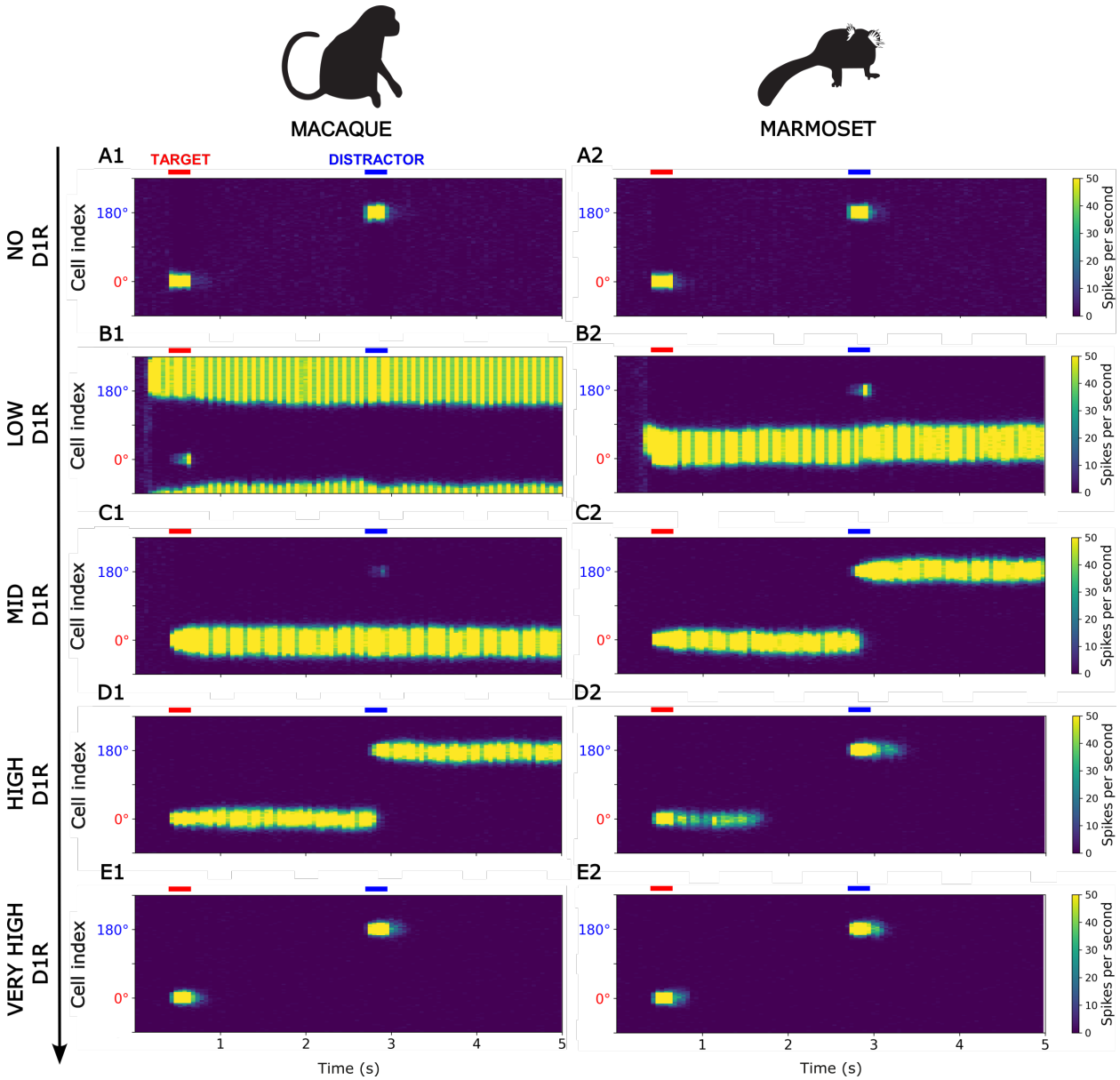

Figure 5 – Distractible, decreasing phase of inverted-U shifted to typical, mid D1R occupancy in the marmoset. Rastergrams represent the color-coded, unmanipulated spike time series for macaque **(A1-E1)** and marmoset **(A2-E2)** of E cells in Network 1, during example five-second trials of the simulated visuospatial working memory task across the five D1R occupancy levels **(A-E)**. E cells are indexed by the angular position from 0° to 360° of their preferred stimulus. The strength of the stimuli is 0.20 pA. For visualization purposes, the y-axis wraps around 270° to accentuate the target (0°) and distractor (180°) positions, and the colour scale is capped to reduce the dominance of outliers in the heatmap, such that any firing rate of >50 Hz per second per neuron is plotted in the same colour as firing rates of 50 Hz.

References

1. Kumita, W., *et al.* Efficient generation of Knock-in/Knock-out marmoset embryo via CRISPR/Cas9 gene editing. *Scientific reports* **9**, 12719 (2019).
2. Oikonomidis, L., *et al.* A dimensional approach to modeling symptoms of neuropsychiatric disorders in the marmoset monkey. *Developmental neurobiology* **77**, 328-353 (2017).
3. Glavis-Bloom, C., Vanderlip, C.R. & Reynolds, J.H. Age-Related Learning and Working Memory Impairment in the Common Marmoset. *J Neurosci* **42**, 8870-8880 (2022).
4. Nakamura, K., *et al.* A Method to Train Marmosets in Visual Working Memory Task and Their Performance. *Frontiers in behavioral neuroscience* **12**, 46 (2018).
5. Miles, R.C. Delayed-response learning in the marmoset and the macaque. *J Comp Physiol Psychol* **50**, 352-355 (1957).
6. Weed, M.R., Bryant, R. & Perry, S. Cognitive development in macaques: attentional set-shifting in juvenile and adult rhesus monkeys. *Neuroscience* **157**, 22-28 (2008).
7. Clarke, H.F., *et al.* Prefrontal serotonin depletion affects reversal learning but not attentional set shifting. *J Neurosci* **25**, 532-538 (2005).
8. Prins, N.W., *et al.* Common marmoset (Callithrix jacchus) as a primate model for behavioral neuroscience studies. *J Neurosci Methods* **284**, 35-46 (2017).
9. Panichello, M.F. & Buschman, T.J. Shared mechanisms underlie the control of working memory and attention. *Nature* **592**, 601-605 (2021).
10. Mendoza-Halliday, D. & Martinez-Trujillo, J.C. Neuronal population coding of perceived and memorized visual features in the lateral prefrontal cortex. *Nature communications* **8**, 15471 (2017).
11. Mendoza-Halliday, D., Xu, H., Azevedo, F.A.C. & Desimone, R. Dissociable neuronal substrates of visual feature attention and working memory. *Neuron* **112**, 850-863.e856 (2024).
12. Goldman-Rakic, P.S. Cellular basis of working memory. *Neuron* **14**, 477-485 (1995).
13. Arnsten, A.F. The neurobiology of thought: the groundbreaking discoveries of Patricia Goldman-Rakic 1937-2003. *Cereb Cortex* **23**, 2269-2281 (2013).
14. Tanaka, S. Computational approaches to the architecture and operations of the prefrontal cortical circuit for working memory. *Progress in Neuro-Psychopharmacology and Biological Psychiatry* **25**, 259-281 (2001).
15. Roussy, M., *et al.* Ketamine disrupts naturalistic coding of working memory in primate lateral prefrontal cortex networks. *Mol Psychiatry* **26**, 6688-6703 (2021).
16. Rao, S.G., Williams, G.V. & Goldman-Rakic, P.S. Destruction and creation of spatial tuning by disinhibition: GABA(A) blockade of prefrontal cortical neurons engaged by working memory. *J Neurosci* **20**, 485-494 (2000).
17. Wilson, F.A., O'Scalaidhe, S.P. & Goldman-Rakic, P.S. Functional synergism between putative gamma-aminobutyrate-containing neurons and pyramidal neurons in prefrontal cortex. *Proc Natl Acad Sci USA* **91**, 4009-4013 (1994).
18. Rao, S.G., Williams, G.V. & Goldman-Rakic, P.S. Isodirectional tuning of adjacent interneurons and pyramidal cells during working memory: evidence for microcolumnar organization in PFC. *J Neurophysiol* **81**, 1903-1916 (1999).
19. Yoshimura, Y. & Callaway, E.M. Fine-scale specificity of cortical networks depends on inhibitory cell type and connectivity. *Nat Neurosci* **8**, 1552-1559 (2005).
20. Runyan, C.A., *et al.* Response features of parvalbumin-expressing interneurons suggest precise roles for subtypes of inhibition in visual cortex. *Neuron* **67**, 847-857 (2010).
21. Wilson, D.E., *et al.* GABAergic Neurons in Ferret Visual Cortex Participate in Functionally Specific Networks. *Neuron* **93**, 1058-1065.e1054 (2017).
22. Wilson, D.E., Scholl, B. & Fitzpatrick, D. Differential tuning of excitation and inhibition shapes direction selectivity in ferret visual cortex. *Nature* **560**, 97-101 (2018).
23. Najafi, F., *et al.* Excitatory and Inhibitory Subnetworks Are Equally Selective during Decision-Making and Emerge Simultaneously during Learning. *Neuron* **105**, 165-179.e168 (2020).

24. Kuan, A.T., *et al.* Synaptic wiring motifs in posterior parietal cortex support decision-making. *Nature* **627**, 367-373 (2024).
25. Znamenskiy, P., *et al.* Functional specificity of recurrent inhibition in visual cortex. *Neuron* **112**, 991-1000.e1008 (2024).
26. Chaplin, T.A., Yu, H.H., Soares, J.G., Gattass, R. & Rosa, M.G. A conserved pattern of differential expansion of cortical areas in simian primates. *J Neurosci* **33**, 15120-15125 (2013).
27. Burman, K.J., Palmer, S.M., Gamberini, M. & Rosa, M.G. Cytoarchitectonic subdivisions of the dorsolateral frontal cortex of the marmoset monkey (Callithrix jacchus), and their projections to dorsal visual areas. *J Comp Neurol* **495**, 149-172 (2006).
28. Kaas, J.H. Comparative Functional Anatomy of Marmoset Brains. *ILAR J* **61**, 260-273 (2020).
29. Elston, G.N., *et al.* Specializations of the granular prefrontal cortex of primates: implications for cognitive processing. *The anatomical record. Part A, Discoveries in molecular, cellular, and evolutionary biology* **288**, 26-35 (2006).
30. Wong, R.K., Selvanayagam, J., Johnston, K.D. & Everling, S. Delay-related activity in marmoset prefrontal cortex. *Cereb Cortex* **33**, 3523-3537 (2023).
31. Vijayraghavan, S., Major, A.J. & Everling, S. Neuromodulation of Prefrontal Cortex in Non-Human Primates by Dopaminergic Receptors during Rule-Guided Flexible Behavior and Cognitive Control. *Front Neural Circuits* **11**, 91 (2017).
32. Crofts, H.S., *et al.* Differential effects of 6-OHDA lesions of the frontal cortex and caudate nucleus on the ability to acquire an attentional set. *Cereb Cortex* **11**, 1015-1026 (2001).
33. Kodama, T., Hikosaka, K., Honda, Y., Kojima, T. & Watanabe, M. Higher dopamine release induced by less rather than more preferred reward during a working memory task in the primate prefrontal cortex. *Behav Brain Res* **266**, 104-107 (2014).
34. Arnsten, A.F., Wang, M. & Paspalas, C.D. Dopamine's Actions in Primate Prefrontal Cortex: Challenges for Treating Cognitive Disorders. *Pharmacol Rev* **67**, 681-696 (2015).
35. Williams, G.V. & Goldman-Rakic, P.S. Modulation of memory fields by dopamine D1 receptors in prefrontal cortex. *Nature* **376**, 572-575 (1995).
36. Wang, M., *et al.* A novel dopamine D1 receptor agonist excites delay-dependent working memory-related neuronal firing in primate dorsolateral prefrontal cortex. *Neuropharmacology* **150**, 46-58 (2019).
37. Vijayraghavan, S., Wang, M., Birnbaum, S.G., Williams, G.V. & Arnsten, A.F. Inverted-U dopamine D1 receptor actions on prefrontal neurons engaged in working memory. *Nat Neurosci* **10**, 376-384 (2007).
38. Gamo, N.J., *et al.* Stress Impairs Prefrontal Cortical Function via D1 Dopamine Receptor Interactions With Hyperpolarization-Activated Cyclic Nucleotide-Gated Channels. *Biol Psychiatry* **78**, 860-870 (2015).
39. Bergson, C., *et al.* Regional, cellular, and subcellular variations in the distribution of D 1 and D 5 dopamine receptors in primate brain. *J Neurosci* **15**, 7821-7836 (1995).
40. Glausier, J.R., Khan, Z.U. & Muly, E.C. Dopamine D1 and D5 receptors are localized to discrete populations of interneurons in primate prefrontal cortex. *Cereb Cortex* **19**, 1820-1834 (2009).
41. Seamans, J.K., Gorelova, N., Durstewitz, D. & Yang, C.R. Bidirectional dopamine modulation of GABAergic inhibition in prefrontal cortical pyramidal neurons. *J Neurosci* **21**, 3628-3638 (2001).
42. Kröner, S., Krimer, L.S., Lewis, D.A. & Barrionuevo, G. Dopamine increases inhibition in the monkey dorsolateral prefrontal cortex through cell type-specific modulation of interneurons. *Cereb Cortex* **17**, 1020-1032 (2007).
43. Jacob, S.N., Stalter, M. & Nieder, A. Cell-type-specific modulation of targets and distractors by dopamine D1 receptors in primate prefrontal cortex. *Nature communications* **7**, 13218 (2016).
44. Glantz, L.A. & Lewis, D.A. Decreased dendritic spine density on prefrontal cortical pyramidal neurons in schizophrenia. *Arch Gen Psychiatry* **57**, 65-73 (2000).
45. Hof, P.R., *et al.* Differential distribution of neurofibrillary tangles in the cerebral cortex of dementia pugilistica and Alzheimer's disease cases. *Acta Neuropathol* **85**, 23-30 (1992).

46. Woo, E., Sansing, L.H., Arnsten, A.F.T. & Datta, D. Chronic Stress Weakens Connectivity in the Prefrontal Cortex: Architectural and Molecular Changes. *Chronic stress* **5**, 24705470211029254 (2021).
47. Nandy, A.S., Sharpee, T.O., Reynolds, J.H. & Mitchell, J.F. The fine structure of shape tuning in area V4. *Neuron* **78**, 1102-1115 (2013).
48. Mitchell, J.F., Reynolds, J.H. & Miller, C.T. Active Vision in Marmosets: A Model System for Visual Neuroscience. *The Journal of Neuroscience* **34**, 1183-1194 (2014).
49. Krienen, F.M.*, et al.* A marmoset brain cell census reveals regional specialization of cellular identities. *Sci Adv* **9**, eadk3986 (2023).
50. Datta, D.*, et al.* Key Roles of CACNA1C/Cav1.2 and CALB1/Calbindin in Prefrontal Neurons Altered in Cognitive Disorders. *JAMA Psychiatry* (2024).
51. Yao, Z.*, et al.* A taxonomy of transcriptomic cell types across the isocortex and hippocampal formation. *Cell* **184**, 3222-3241 e3226 (2021).
52. Ma, S.*, et al.* Molecular and cellular evolution of the primate dorsolateral prefrontal cortex. *Science*, eabo7257 (2022).
53. Paspalas, C.D. & Goldman-Rakic, P.S. Microdomains for dopamine volume neurotransmission in primate prefrontal cortex. *J Neurosci* **24**, 5292-5300 (2004).
54. Paspalas, C.D. & Goldman-Rakic, P.S. Presynaptic D1 dopamine receptors in primate prefrontal cortex: target-specific expression in the glutamatergic synapse. *J Neurosci* **25**, 1260-1267 (2005).
55. Compte, A., Brunel, N., Goldman-Rakic, P.S. & Wang, X.J. Synaptic mechanisms and network dynamics underlying spatial working memory in a cortical network model. *Cereb Cortex* **10**, 910-923 (2000).
56. Tanaka, S. Architecture and dynamics of the primate prefontal coritical circuit for spatial working memory. *Neural Networks* **12**, 1007-1020 (1999).
57. Roach, J.P., Churchland, A.K. & Engel, T.A. Choice selective inhibition drives stability and competition in decision circuits. *Nature communications* **14**, 147 (2023).
58. Lim, S. & Goldman, M.S. Balanced cortical microcircuitry for maintaining information in working memory. *Nat Neurosci* **16**, 1306-1314 (2013).
59. Xue, C. & Liu, F. Structured synaptic inhibition has a critical role in multiple-choice motion-discrimination tasks. *J Neurosci* **34**, 13444-13457 (2014).
60. Lagzi, F., Bustos, M.C., Oswald, A.-M. & Doiron, B. Assembly formation is stabilized by Parvalbumin neurons and accelerated by Somatostatin neurons. *bioRxiv*, 2021.2009.2006.459211 (2021).
61. Seamans, J.K., Durstewitz, D., Christie, B.R., Stevens, C.F. & Sejnowski, T.J. Dopamine D1/D5 receptor modulation of excitatory synaptic inputs to layer V prefrontal cortex neurons. *Proc Natl Acad Sci USA* **98**, 301-306 (2001).
62. Durstewitz, D., Seamans, J.K. & Sejnowski, T.J. Dopamine-mediated stabilization of delay-period activity in a network model of prefrontal cortex. *J Neurophysiol* **83**, 1733-1750 (2000).
63. Gonzalez-Burgos, G., Kroener, S., Seamans, J.K., Lewis, D.A. & Barrionuevo, G. Dopaminergic modulation of short-term synaptic plasticity in fast-spiking interneurons of primate dorsolateral prefrontal cortex. *J Neurophysiol.* **94**, 4168-4177 (2005).
64. Gao, W.J. & Goldman-Rakic, P.S. Selective modulation of excitatory and inhibitory microcircuits by dopamine. *Proc Natl Acad Sci USA* **100**, 2836-2841 (2003).
65. Williams, G.V. & Castner, S.A. Under the curve: critical issues for elucidating D1 receptor function in working memory. *Neuroscience* **139**, 263-276 (2006).
66. Lagzi, F. & Fairhall, A.L. Emergence of co-tuning in inhibitory neurons as a network phenomenon mediated by randomness, correlations, and homeostatic plasticity. *Sci Adv* **10**, eadi4350 (2024).
67. Suzuki, M. & Gottlieb, J. Distinct neural mechanisms of distractor suppression in the frontal and parietal lobe. *Nat Neurosci* **16**, 98-104 (2013).
68. Brozoski, T.J., Brown, R.M., Rosvold, H.E. & Goldman, P.S. Cognitive deficit caused by regional depletion of dopamine in prefrontal cortex of rhesus monkey. *Science* **205**, 929-932 (1979).

69. Sawaguchi, T. & Goldman-Rakic, P.S. D1 dopamine receptors in prefrontal cortex: involvement in working memory. *Science* **251**, 947-950 (1991).
70. Durstewitz, D. & Seamans, J.K. The dual-state theory of prefrontal cortex dopamine function with relevance to catechol-o-methyltransferase genotypes and schizophrenia. *Biol Psychiatry* **64**, 739-749 (2008).
71. Li, Y.C., Liu, G., Hu, J.L., Gao, W.J. & Huang, Y.Q. Dopamine D(1) receptor-mediated enhancement of NMDA receptor trafficking requires rapid PKC-dependent synaptic insertion in the prefrontal neurons. *J Neurochem* **114**, 62-73 (2010).
72. Paspalas, C.D., Wang, M. & Arnsten, A.F. Constellation of HCN channels and cAMP regulating proteins in dendritic spines of the primate prefrontal cortex: potential substrate for working memory deficits in schizophrenia. *Cereb Cortex* **23**, 1643-1654 (2013).
73. Almeida, R., Barbosa, J. & Compte, A. Neural circuit basis of visuo-spatial working memory precision: a computational and behavioral study. *J Neurophysiol* **114**, 1806-1818 (2015).
74. Nassar, M.R., Helmers, J.C. & Frank, M.J. Chunking as a rational strategy for lossy data compression in visual working memory. *Psychol Rev* **125**, 486-511 (2018).
75. Barbosa, J.*, et al.* Interplay between persistent activity and activity-silent dynamics in the prefrontal cortex underlies serial biases in working memory. *Nat Neurosci* **23**, 1016-1024 (2020).
76. Barbosa, J., Babushkin, V., Temudo, A., Sreenivasan, K.K. & Compte, A. Across-Area Synchronization Supports Feature Integration in a Biophysical Network Model of Working Memory. *Front Neural Circuits* **15**, 716965 (2021).
77. Furman, M. & Wang, X.J. Similarity effect and optimal control of multiple-choice decision making. *Neuron* **60**, 1153-1168 (2008).
78. Ardid, S., Wang, X.J. & Compte, A. An integrated microcircuit model of attentional processing in the neocortex. *J Neurosci* **27**, 8486-8495 (2007).
79. Edin, F.*, et al.* Mechanism for top-down control of working memory capacity. *Proc Natl Acad Sci USA* **106**, 6802-6807 (2009).
80. Ardid, S., Wang, X.J., Gomez-Cabrero, D. & Compte, A. Reconciling coherent oscillation with modulation of irregular spiking activity in selective attention: gamma-range synchronization between sensory and executive cortical areas. *J Neurosci* **30**, 2856-2870 (2010).
81. Wei, Z., Wang, X.J. & Wang, D.H. From distributed resources to limited slots in multiple-item working memory: a spiking network model with normalization. *J Neurosci* **32**, 11228-11240 (2012).
82. Brunel, N. & Wang, X.J. Effects of neuromodulation in a cortical network model of object working memory dominated by recurrent inhibition. *J Comput Neurosci* **11**, 63-85 (2001).
83. Tanaka, S. Dopaminergic control of working memory and its relevance to schizophrenia: a circuit dynamics perspective. *Neuroscience* **139**, 153-171 (2006).
84. Loh, M., Rolls, E.T. & Deco, G. A dynamical systems hypothesis of schizophrenia. *PLoS Comput Biol* **3**, e228 (2007).
85. Okimura, T., Tanaka, S., Maeda, T., Kato, M. & Mimura, M. Simulation of the capacity and precision of working memory in the hypodopaminergic state: Relevance to schizophrenia. *Neuroscience* **295**, 80-89 (2015).
86. Reneaux, M., Gupta, R. & Karmeshu. Stochastic Mesocortical Dynamics and Robustness of Working Memory during Delay-Period. *PLoS One* **10**, e0144378 (2015).
87. Reneaux, M. & Gupta, R. Prefronto-cortical dopamine D1 receptor sensitivity can critically influence working memory maintenance during delayed response tasks. *PLoS One* **13**, e0198136 (2018).
88. Froudist-Walsh, S.*, et al.* A dopamine gradient controls access to distributed working memory in the large-scale monkey cortex. *Neuron* **109**, 3500-3520 e3513 (2021).
89. Gao, W.J., Wang, Y. & Goldman-Rakic, P.S. Dopamine modulation of perisomatic and peridendritic inhibition in prefrontal cortex. *J Neurosci* **23**, 1622-1630 (2003).
90. Anastasiades, P.G., Boada, C. & Carter, A.G. Cell-Type-Specific D1 Dopamine Receptor Modulation of Projection Neurons and Interneurons in the Prefrontal Cortex. *Cereb Cortex* **29**, 3224-3242 (2019).

91. Wang, X.J., Tegner, J., Constantinidis, C. & Goldman-Rakic, P.S. Division of labor among distinct subtypes of inhibitory neurons in a cortical microcircuit of working memory. *Proc Natl Acad Sci USA* **101**, 1368-1373 (2004).
92. Torres-Gomez, S.*, et al.* Changes in the Proportion of Inhibitory Interneuron Types from Sensory to Executive Areas of the Primate Neocortex: Implications for the Origins of Working Memory Representations. *Cereb Cortex* **30**, 4544-4562 (2020).
93. Kvitsiani, D.*, et al.* Distinct behavioural and network correlates of two interneuron types in prefrontal cortex. *Nature* **498**, 363-366 (2013).
94. Ghaderi, P., Marateb, H.R. & Safari, M.S. Electrophysiological Profiling of Neocortical Neural Subtypes: A Semi-Supervised Method Applied to in vivo Whole-Cell Patch-Clamp Data. *Front Neurosci* **12**, 823 (2018).
95. DeFelipe, J. Types of neurons, synaptic connections and chemical characteristics of cells immunoreactive for calbindin-D28K, parvalbumin and calretinin in the neocortex. *J Chem Neuroanat* **14**, 1-19 (1997).
96. Yang, G.R., Murray, J.D. & Wang, X.J. A dendritic disinhibitory circuit mechanism for pathway-specific gating. *Nature communications* **7**, 12815 (2016).
97. Krabbe, S.*, et al.* Adaptive disinhibitory gating by VIP interneurons permits associative learning. *Nat Neurosci* **22**, 1834-1843 (2019).
98. Dzaja, D., Hladnik, A., Bicanic, I., Bakovic, M. & Petanjek, Z. Neocortical calretinin neurons in primates: increase in proportion and microcircuitry structure. *Front Neuroanat* **8**, 103 (2014).
99. Lammel, S., Ion, D.I., Roeper, J. & Malenka, R.C. Projection-specific modulation of dopamine neuron synapses by aversive and rewarding stimuli. *Neuron* **70**, 855-862 (2011).
100. Finlay, J.M., Zigmond, M.J. & Abercrombie, E.D. Increased dopamine and norepinephrine release in medial prefrontal cortex induced by acute and chronic stress: effects of diazepam. *Neuroscience* **64**, 619-628 (1995).
101. Murphy, B.L., Arnsten, A.F.T., Goldman-Rakic, P.S. & Roth, R.H. Increased dopamine turnover in the prefrontal cortex impairs spatial working memory performance in rats and monkeys. *Proc Natl Acad Sci USA* **93**, 1325-1329 (1996).
102. Qin, S.*, et al.* The effect of moderate acute psychological stress on working memory-related neural activity is modulated by a genetic variation in catecholaminergic function in humans. *Frontiers in integrative neuroscience* **6**, 16 (2012).
103. Holtzman, C.W.*, et al.* Stress and neurodevelopmental processes in the emergence of psychosis. *Neuroscience* **249**, 172-191 (2013).
104. Robinson, M.D., McCarthy, D.J. & Smyth, G.K. edgeR: a Bioconductor package for differential expression analysis of digital gene expression data. *Bioinformatics* **26**, 139-140 (2009).

Online Methods:

Behavior

Subjects: Eight marmosets (age ranging 2-7 years, 7 male and 1 female) and two macaques (age ranging 10-15 years, both male) were used. All experiments in marmosets were approved by the Institutional Animal Care and Use Committees at their respective institutions which included 5 males and 1 female at the University of Rochester, New York, and two males at the University of California, San Diego, that were part of a previous study[1]. All procedures in macaques were approved by the Salk Institute Institutional Animal Care and Use Committee and conformed to NIH guidelines. Fixation data from previously published studies were reanalyzed in the two macaques[2] and from two male marmosets[1], while new data from 6 additional marmosets trained in the same task as the original two marmosets have been contributed for this study.

Testing: To quantify the difference in distractibility between marmosets and macaques we compared data collected from previous studies in marmosets and macaques that used a similar basic fixation task, with no motor demands and minimal cognitive load, where the subjects ignored peripherally flashed distractors to maintain central fixation. This task is commonly used to map receptive field properties of neurons in visual areas with rhesus macaques[2], and it has been shown that marmosets can also perform similar fixation tasks[1]. Both species underwent similar training protocols to learn how to acquire fixation on a central point and then hold it through a period in which distractors were flashed in the periphery. All subjects in the present study had been previously trained on the task during receptive field mapping for visual tasks. They were thus acclimated to the task, which precluded a learning component in the testing sessions used for the present study. Macaques and marmosets viewed a centrally presented fixation point (~0.2-0.3° radius, at 100% contrast) on a video display at 57 cm distance while their eye position was monitored with an infra-red eye tracker. After calibration of the eye tracker, monkeys were required to maintain fixation within a 1-2° radius window around the central point. In each task trial fixation was first obtained within the fixation window and held for a minimum duration of 100 ms, after which a set of Gabor edge stimuli were flashed at peripheral positions. The flashed Gabor stimuli were 1-2° in diameter and had a spatial frequency between 1-2 cycles per degree. They were drawn at random from 8 orientations and shown at 100% Michelson contrast against a grey background. The flashed stimuli could appear at randomly selected positions ranging between +/-15 visual degrees on the vertical and horizontal but not within 2° of the fixation point. They were updated in position at each video frame at a rate of 60 Hz. Monkeys were rewarded with a drop of juice for holding fixation at increasingly longer epochs up to a maximum delay of 3 seconds. During initial training the minimum hold duration for reward was gradually increased per behavioral session for macaques until they saturated in performance for their held fixation duration. In the case of marmosets, the fixation duration was also gradually increased, but done so within a behavioral session using a 1-up 1-down staircase procedure where the duration increased after each successful hold trial and decreased upon a failed trial, and where the amount of juice reward provided was in proportion to the duration of the hold.

Data Analysis and Statistics: Data used to estimate hold durations was taken after initial training had reflected a saturation in performance. After performance saturated a minimum of 8 behavioral sessions with a minimum of 200 completed fixation trials was collected. We computed the mean fixation hold and standard deviation for each animal. Mean hold durations between macaques and marmosets were compared for a difference in median mean duration using a Ranksum test.

Single nucleus RNA sequencing of DRD1 in PVALB neuron clusters of dlPFC comparing macaques and marmosets

Single nucleus cortical GABAergic neuron data were obtained and reanalyzed from a prior study by Krienen *et al.*[3]. Single nucleus RNA sequencing data from macaque cortical GABAergic neurons was obtained from a dataset from which only glutamatergic neurons have been previously analyzed[4].

Information about the subjects used for this study and sequencing procedures can be found for marmosets[5] and macaques[4]. Briefly, marmosets (n = 12, sex = 7F, 5M, age range 2-14 years) were cared for and housed at the Broad Institute in Cambridge, MA and all procedures were approved by the Massachusetts Institute for Technology Committee for Animal Care (CAC) guidelines. Macaques (n = 2, both female, age range 6-8 years) were cared for and housed at the University of Pittsburgh in Pittsburgh, PA and all procedures were approved by the University of Pittsburgh Institutional Animal Care and Use Committee (IACUC).

Fresh-frozen postmortem macaque dlPFC tissue containing both banks of the principal sulcus area 46 was obtained from two experimentally-naïve, female, adult (6.6 and 8.2 years of age) Rhesus macaque monkeys at the University of Pittsburgh. Animals were deeply anesthetized and perfused with artificial cerebral spinal as previously described[4] in accordance with USDA and NIH guidelines and with the approval of the University of Pittsburgh IACUC.

Single nucleus RNA sequencing was performed on marmoset and macaque dlPFC tissues using the 10x Chromium 3' v3 and v3.1 chemistry. Nuclei suspensions, library preparation, sequencing and preprocessing for marmoset is described in Krienen *et al.*[3] and macaque by Datta *et al.*[4]. Marmoset data were aligned to genome CJ1700 from NCBI; macaque data were aligned to reference Mmul10.

Analysis and QC was performed as previously described[3, 4]. Briefly, nuclei with fewer than 500 genes or 1000 transcripts were removed from the analysis. Independent component analysis (ICA, using the fastICA package in R) was performed on all cells, using the filtered digital gene expression matrix (DGE) after normalization and variable gene selection following procedures described in Saunders *et al.*[6] and Krienen *et al.*[7]. Louvain clustering (resolution 0.1, nearest neighbors = 25) was performed using the top 60 ICs. ICA and Louvain clustering was repeated on each of the neuron clusters, resulting in further subdivisions of the major types. Cell and gene weights on independent components (ICs) were manually inspected for evidence of cell-cell doublets or non-neurons, both of which were removed from the DGE. ICs that reflected artifactual signals or batch effects were identified and excluded, and Louvain clustering was performed on the retained ICs. Within each cluster, transcripts for each gene were summed across cells of that cluster. The resulting "metacell" counts were normalized to the total number of transcripts, then scaled to counts per 100,000 and log10 transformed.

For each species (marmoset, macaque), cortical GABAergic clusters were identified based on the expression of GABAergic neuron markers (*GAD1*, *GAD2*, *RBFOX3*), and carried forward for further analysis. Expression levels per 100k transcripts were averaged over *PVALB* clusters if there were more than one detected.

Evolutionary transcriptomics

To plot phylogenetic trends in *DRD1* expression in PFC *PVALB* neurons, we statistically compared its expression in mice, non-human primates and humans. We first downloaded the processed single-nucleus RNA-seq data from adult primates (i.e., human, rhesus macaque and marmoset) dlPFC[8]. Because the dlPFC is unique to primates, we included the single-cell transcriptomics data from analogous mouse areas PL-IL-ORB (prelimbic, infralimbic and orbital regions) regions[9]. The *PVALB* neuron populations were extracted from both datasets.

To account for the biological variation present among donors of each species, we aggregated the UMI (unique molecular identifier) counts of *PVALB* neurons in each donor via pseudobulking strategy[10]. We then subset the data using the ortholog genes identified via orthogene package[11] and conducted different gene expression test using edgeR package[12]. The ortholog genes were also leveraged to compute the library size in each pseudobulk sample followed by library size normalization and log2 transformation, using the following equation:

$$x_j = log_2(\frac{c_j \times s}{l} + 1)$$

Here, the x_j represents the log2-normalized expression of a given gene j, c_j refers to the unique molecular identifier (UMI) counts for the gene j, s is the scaling factor (1000,000 was used here), and l denotes the library size.

Evaluation of in situ protein expression of D1R in PV neurons of dlFPC

Subjects: Tissue for analysis of D1R protein-level expression in macaques was obtained from our extant brain bank from the Yale colony of rhesus macaques (*Macaca mulatta*). All research was approved by the Yale IACUC and was in compliance with NIH and NSF regulations. Animals were perfused with 0.1M phosphate buffer, followed by 4% paraformaldehyde and 0.05% glutaraldehyde in 0.1M PB, for concurrent studies conducted requiring fixation protocols for electron microscopy. For each subject, a craniotomy was performed, and the entire brain was removed, including a dorsolateral block containing the principal sulcus. Blocks were sectioned coronally at 60µm on a vibratome (Leica VT100S). Sections were cryoprotected through increasing concentrations of sucrose solution (10%, 20% and 30% each overnight), cooled rapidly using liquid nitrogen and stored at -80°C. To enable penetration of immunoreagents, all sections were subjected to three freeze-thaw cycles in liquid nitrogen. Sections from the dlPFC of two female young adult macaques aged 8 and 10 years were used in this study. We isolated sections with the principal sulcus and imaged in the dorsal or ventral bank of the principal sulcus, approximately midway through its anterior-posterior axis.

Tissue in marmosets was obtained from University of Western Ontario, where all experimental procedures were performed in accordance with the Canadian Council on Animal Care guidelines and approved by the University of Western Ontario Animal Use Subcommittee (AUP: 20180130) and in accordance with NSF regulations. One male and one female (both aged 5 years) young adult marmosets were perfused with 4% paraformaldehyde and 0.05% glutaraldehyde in 100mM PBS, and postfixed in 4% paraformaldehyde in 0.1M PBS for 24 hrs and blocked. Dorsolateral blocks were cut on a vibratome into 50 um sections and collected serially, and stored long-term at -20°C in cryoprotectant composed of 30% glycerol, 30% ethylene glycol in 0.1M PB. For immunohistochemistry, we sampled sections containing A46d and A46v, guided by the location of delay-related neuronal firing correlated with working memory[13].

Antibody selection and validation: D1R labeling in macaques has been performed for decades using a knockout-validated[14] antibody (Sigma rat anti-D1R, cat# D2944) against the human D1R. This antibody is known for producing a patchy pattern of labeling in neurons, which has been attributed to its robust labeling in the Golgi apparatus[15-17]. We found that this antibody performed differently in the marmoset, producing a qualitatively distinct labeling pattern from the macaque. The labeling in the marmoset did not exhibit the characteristic patchy Golgi-like pattern well-documented in the macaque, and which we observed in our macaque tissue. The marmoset labeling pattern entirely filled the cytoplasm of labeled neurons and also labeled what appeared to be glia. This discrepancy may be due to two amino acid residue sequence differences between macaques and marmosets in the epitope region of the D1R that is bound by the Sigma antibody. We then optimized the second-best performing antibody from knockout validation[14], the Alomone rabbit anti-D1R (cat# ADR-001), which has been used successfully in macaque tissue for immunofluorescence[18], and produced satisfactory and comparable labeling in our macaque and marmoset tissue, although without the characteristic Golgi-like labeling pattern observed by the Sigma antibody. The Alomone antibody was generated against an epitope on the intracellular C-terminus of the rat D1R (amino acid residues 372-385). The amino acid residues in the epitope sequence are conserved in marmosets and macaques. We used the Alomone D1R blocking peptide (cat# BLP-DR001) as a negative preadsorption control, described more fully below.

Immunohistochemistry: Both species were processed together using the same solutions to ensure identical treatment. Free-floating sections were removed from long-term storage and washed in phosphate buffer (0.1M PB, 4x15 min), followed by an incubation for 1 hr in glycine (50 mM in 0.1M PB, room temperature, Sigma, cat# G-7126) to bind free aldehydes, PB washes (4x15 min), and Avidin Biotin blocking (Vector, cat# SP-2001) to block any endogenous biotin. Following more PB washes (4x15 min), the tissue was incubated for 1 hr at room temperature in a blocking solution of 5% bovine serum albumin (AmericanBio, cat# 9048-46-8), 10% normal goat serum (Jackson ImmunoResearch, cat# 005-00-001), and 2% Triton X-100 (Electron Microscopy Sciences, cat# 22140) in 0.1M PB. Tissue was then incubated for 72 hrs at 4°C in PB with rabbit anti-D1R (1:100, Alomone, cat# ADR-001), and guinea pig anti-PV (1:2000, Swant, cat# GP72). Tissue was then washed in PB (4x15 min) and incubated for 3 hrs at room temperature in PB with Alexa Fluor-488 goat anti-rabbit (1:100, Invitrogen, cat# A11008) and Alexa Fluor-568 goat anti-guinea pig (1:100, Invitrogen, cat# A11075). Sections were then washed with PB (4x15 min), and mounted onto slides using Prolong Gold Antifade (Invitrogen, cat# P36930), dried, coverslipped, and sealed with fast-drying nail polish. A control piece of tissue was treated as above, except for the primary antibody incubation step, which additionally included the Alomone D1R antigen blocking peptide (cat# BLP-DR001) at 10x the D1R antibody concentration (pre-incubated for 1 hr). Upon imaging, no specific labeling was observed in the D1R channel in the control section (Figure S3), validating the specificity of the antibody's paratope in its interactions with our sections.

We also performed additional immunofluorescence labeling, depicted in Figure S1. D1R and PV labeling procedures were performed as above with the addition of microtubule-associated protein 2 (MAP2) and the nuclear Hoechst stain. The primary antibody incubation included the addition of a chicken anti-MAP2 (Abcam, cat# AB5392, 1:1000), and the secondary antibody incubation included goat anti-chicken Alexa Fluor-647 (1:100, Invitrogen cat# A21449). The Hoechst nuclear stain was included at the end at 1:10,000 (Fisher Scientific, cat# H3570).

Sampling and Imaging: In layer IIIb, 5-10 sampling sites were imaged per section, sometimes capturing almost all of the marmoset 46d or 46v layer III in section, and in macaque utilizing every other field of view traversing along deep layer III parallel to the pia. Layers were determined at a lower magnification

objective using the pattern of pyramidal D1R labeling, and PV labeling, which is specific to laminar compartments[19]. Confocal images for marmosets and macaques were acquired during the same session using a Zeiss LSM880 Airyscan with the Plan-Apochromat 20x/0.8 M27 or C-Apochromat 40x/1.2W Korr FCS M27 objectives. Z-stacks at various z-steps were obtained under sequential excitation at 488 nm, and 561 nm. After initially surveying sections from both species, imaging parameters (laser power, gain settings, pinhole, etc.) were set at the start so that images acquired across species were subject to equivalent imaging parameters. Parameters were optimized for focal planes near the top and bottom of the tissue section, as D1R antibody penetration was attenuated in the middle depths of the sections for both species, and to avoid pixel saturation. Images were deconvolved using Huygens Professional version 22.04 (Scientific Volume Imaging, The Netherlands) using as uniform parameters as possible (theoretical PSF, classic MLE algorithm, SNR set at ~15, background set at 0, and acuity optimized for smoothness). We used Fiji[20] to further analyze all deconvolved images. The D1R signal was optimal in a window of ~15 µm from the top or bottom of the section. Two single focal planes from each stack were extracted, one each from the optimal sectors at the top or bottom of the section, while ensuring that no neuronswere present in both and avoiding the absolute top or bottom due to the presence of surface artefacts. Extracted focal planes were used for two independent analyses, discussed sequentially below. We sampled from 4 sections per subject. In total, we analyzed ~100 images, encompassing ~400-500 PV neurons per subject.

Analysis of D1R expression in PV processes: To perform the colocalization analysis, we used the EZColocalization plugin[21, 22]. For each extracted focal plane, we performed particle segmentation to isolate PV neurons and dendrites, utilizing either the Renyi or Otsu thresholding methods, producing sometimes over a thousand particles per image, including both dendritic and somatic segments. An areal filter was applied so particles smaller than 0.55 μm^2 were excluded. Segmented particles were analyzed manually to classify into two categories, i) PV neuron somata and/or proximal dendritic segments, which were sometimes continuous; or ii) non-proximal PV dendrites. Any quantal isolated signals that could not be traced to a continuous dendrite were discarded and proximal dendrites were identified as being readily traced back to a PV+ neuron soma. The areal segmentation filter and manual identification helped exclude PV+ thalamocortical axons that may have been present within the section. For each focal plane, PV+ particles were then analyzed for colocalization using the Costes' thresholding method and Manders' Overlap Coefficient (MOC). Briefly, the Costes' thresholding identifies pixels that qualify as colocalized for each image, and the MOC roughly computes the proportion of colocalized pixels among total pixels contained in a PV particle. We ran a separate Costes' and MOC analysis on a subset of manually segmented PV particles and received consistent results with the automatically segmented set.

Then, we performed a separate independent analysis of D1R labeling in manually traced PV neuron somata. This is because the automated segmentation often produced multiple segments per PV soma, and included dendritic PV segments present in the image. For each image, we isolated the D1R channel and manually traced the 3-6 most strongly D1R labeled somata in the image, which were typically pyramidal-like in morphology. We then sampled 10-20 segments of the immunonegative "neuropil". In the isolated D1R channel, we measured the mean grey value (MGV) for the strongly labeled D1R somata traces and the sampled neuropil traces. We then used the minimum MGV across the "strong" D1R traces, and the average MGV across D1R "neuropil" traces to compute two bins of intermediate D1R labeling between the average MGV in the neuropil and the minimum MGV from the strongly labeled D1R traces. In this way, we were able to normalize for the illumination level of each image. Then, in the isolated PV channel of the same image, we traced the outlines of the PV somata, measured the D1R MGV for each traced PV somata, and classified the PV somata as having a D1R MGV i) below the average MGV in the neuropil, deemed "D1R negative", ii) in two intermediate bins, "D1 weak" or "D1 moderate", or iii) above the

minimum MGV observed among the "strongly" labeled D1R somata. This strategy has been schematized in Figure S2. We analyzed a total of 1,821 PV neuronal somata across all sampled focal planes (Marm1: n = 512 PV neurons; Marm2, n = 501; Mac2, n = 403; Mac1, n = 405).

Brightness and contrast adjustments were made for qualitative figures using Fiji or Adobe Photoshop CS5 Extended (version 12.0.4x64, Adobe Systems Incorporated), though all quantitative analysis was performed on untouched images straight after deconvolution. Figures were prepared in Adobe Illustrator CC.2020.01 (Adobe Systems Incorporated).

Statistical Analysis: Statistical analysis was performed using Prism 9 (Graphpad Software, LLC). To remove independence violations, we analyzed the data using the mean per subject. We checked the assumptions for parametric tests, and used a t-test to test the mean MOC across species, and a two-way ANOVA with post-hoc Sidak's corrected pairwise comparisons to test the effects of species and effect of proximity to soma, and interaction between the two. Means are reported with standard deviation, when appropriate, as indicated in the text and plots.

Computational Modeling

Microcircuit architecture: The three main spiking neural networks comprise 2048 near feature-tuned, regular-spiking excitatory (E) Delay cells, 256 near feature-tuned, fast-spiking inhibitory (I_{NEAR}) Delay cells, and 256 opposite feature-tuned, fast-spiking inhibitory (I_{OPP}) Delay cells. Alternatively, in addition to 2048 E cells, the I cells in the I_{NEAR}-only network represent only 512 I_{NEAR} cells, while in the I_{OPP}-only network, they represent only 512 I_{OPP} cells. Each cell type uniformly covers all angles θ on a ring in feature space from 0° to 360° (Figure 4A1). E cells are indexed by the angular position of the visual stimuli to which they respond preferentially with the highest strength, while I cells conform to the indexing of the E cells from which they receive the strongest excitation.

Single-cell model: We modelled all cells as single-compartment leaky integrate-and-fire units characterised by the following intrinsic parameters: total membrane capacitance (C_m), total leak conductance (g_L), leak reversal potential (E_L), the firing threshold potential (V_{th}), the reset potential (V_{res}), and the refractory time (τ_{ref})[23]. For E and I cells, the parameter values used in simulations are listed in Table 1[24, 25]. The change in the subthreshold membrane voltage V at a given time point t of each postsynaptic cell i, denoted as $V_i(t)$, is given by:

$$C_m \frac{dV_i(t)}{dt} = -g_L(V_i(t) - E_L) - I_i(t), \qquad \text{Eq. (1)}$$

where $I_i(t)$ is the total input current to the cell.

Receptor dynamics: Cells receive recurrent excitatory inputs through α-amino-3-hydroxy-5-methyl-4-isoxazolepropionic acid receptor (AMPAR)- and N-methyl-D-aspartate receptor (NMDAR)-mediated synaptic current transmissions and inhibitory inputs through gamma-aminobutyric acid type A receptor ($GABA_AR$)-mediated synaptic current transmissions. The total input current to a given postsynaptic cell, $I_i(t)$, is:

$$I_i(t) = I_{i,\mathrm{AMPA}}(t) + I_{i,\mathrm{NMDA}}(t) + I_{i,\mathrm{GABA}_A}(t) + I_{i,stim}(t), \quad \text{Eq. (2)}$$

where $I_{i,stim}$ designates the external stimulus input to the cell (see Eq. 15).

We modelled the dynamics of the receptor-specific synaptic input currents for each postsynaptic cell at a given time point, denoted as $I_{i,r}(t)$, based on Wang[25], as follows:

$$I_{i,\mathrm{AMPA}}(t) \;=\; (V_i(t) \;-\; V_E) \sum_j g_{ij,\mathrm{AMPA}}\; s_{j,\mathrm{AMPA}}(t), \quad \text{Eq. (3)}$$

$$I_{i,\mathrm{NMDA}}(t) \;=\; (V_i(t) \;-\; V_E) \sum_j \frac{g_{ij,\mathrm{NMDA}}\; s_{j,\mathrm{NMDA}}(t)}{1 \;+\; [\mathrm{Mg}^{2+}] \exp\left(-0.062 V_i(t)\right)/3.57}, \quad \text{Eq. (4)}$$

$$I_{i,\mathrm{GABA}_A}(t) \;=\; (V_i(t) \;-\; V_I) \sum_j g_{ij,\mathrm{GABA}_A}\; s_{j,\mathrm{GABA}_A}(t), \quad \text{Eq. (5)}$$

where $g_{ij,r}$, $r \in \{AMPA, NMDA, GABA_A\}$, is the maximum receptor-specific conductance at the connection between presynaptic and postsynaptic cells j and i. $s_{j,r}(t)$ is the contribution to the receptor-specific synaptic gating variable by a given presynaptic cell at a given time point. V_E and V_I are the reversal potentials for the excitatory AMPAR and NMDAR channels and the inhibitory GABA_AR channels (Table 2). $V_i(t)$ is the membrane potential at a given time point. The NMDAR-mediated excitatory postsynaptic currents exhibit voltage dependence governed by the extracellular concentration of magnesium, $[\mathrm{Mg}^{2+}]$ (Table 2)[26].

We modelled the AMPAR and GABA_AR synaptic gating variables as instantaneous jumps of magnitude 1 when a presynaptic spike occurs, followed by a fast exponential decay with time constants τ_{AMPA}[27, 28] and τ_{GABA_A}[29, 30] (Table 2). The gating variables for AMPAR and GABAR channels are, thus, given by:

$$\frac{ds_{\mathrm{AMPA}}(t)}{dt} = -\frac{s_{\mathrm{AMPA}}(t)}{\tau_{\mathrm{AMPA}}} + \sum_k \delta_{\mathrm{rec}}(t - t_k), \quad \text{Eq. (6)}$$

$$\frac{ds_{\mathrm{GABA}_A}(t)}{dt} \;=\; -\frac{s_{\mathrm{GABA}_A}(t)}{\tau_{\mathrm{GABA}_A}} \;+\; \sum_k \delta_{\mathrm{rec}}(t - t_k), \quad \text{Eq. (7)}$$

whereas the gating variable for NMDAR channels is given by:

$$\frac{ds_{\mathrm{NMDA}}(t)}{dt} \;=\; -\;\frac{s_{\mathrm{NMDA}}(t)}{\tau_{\mathrm{NMDA}}} \;+\; \alpha_s\, x(t)\,(1 \;-\; s_{\mathrm{NMDA}}(t)), \quad \text{Eq. (8)}$$

$$\frac{dx(t)}{dt} \;=\; -\frac{x(t)}{\tau_x} \;+\; \sum_k \delta_{\mathrm{rec}}(t - t_k), \quad \text{Eq. (9)}$$

where x is an intermediate gating variable proportional to the glutamate concentration in the synapse, τ_{NMDA} is the slow decay time constant of NMDAR-mediated postsynaptic currents, τ_x is the rise time constant of NMDAR channels, and α_s is the presynaptic firing frequency at which NMDAR channels saturate and become insensitive to further frequency increases (Table 2). Across equations, δ_{rec} denotes the Dirac delta functions that represent the arrival of the spikes from the presynaptic, recurrent sources at times t_k.

To simulate background noise (e.g., from other cortical areas), we applied 1000 random, exclusively AMPAR-mediated, external excitatory inputs to each cell as uncorrelated presynaptic Poisson spike trains. Each train had a firing rate of 1.8 Hz, with conductances of $g_{\mathrm{ext\rightarrow E,\ AMPA}}$ and $g_{\mathrm{ext\rightarrow I,\ AMPA}}$ on E and I cells (Table 4).

Synaptic connectivity: The microcircuit model features E→E (Figure 4A2), E→I, I→E (Figure 4A3-4), and I→I synaptic connections. Excluding autapses, we assume all-to-all connectivity between cells for each connection type. E cells innervate with their strongest glutamatergic projections cells of all types that occupy the nearest angular positions. I_{NEAR} cells recapitulated the targeting of E cells, while for I_{OPP} cells, the targeting is rotated by 180°. Thus, I_{NEAR} cells innervate with their strongest GABAergic projections cells of all types that also occupy the nearest angular position, while I_{OPP} cells – cells of all types positioned 180° away on the ring.

The receptor conductance, denoted as $g_{ij,r}$ at a connection between the presynaptic and postsynaptic cells j and i is given by:

$$g_{ij,r} = W_{\mathrm{syn}}(\theta_i - \theta_j) G_{\mathrm{syn},r}, \qquad \text{Eq. (10)}$$

where $G_{\mathrm{syn},r}$ is the mean receptor-specific conductance at the given synaptic connection type, weighted by a Gaussian distribution of the difference between the angular positions θ_i and θ_j of the preferred stimuli of the postsynaptic and presynaptic cells:

$$W_{\mathrm{syn}}(\theta_i - \theta_j) = J^{-}_{\mathrm{syn}} + \left(J^{+}_{\mathrm{syn}} - J^{-}_{\mathrm{syn}}\right) \exp\left[-\frac{(\theta_i - \theta_j - \Theta^{\mathrm{shift}}_{\mathrm{syn}})^2}{2\sigma^2_{\mathrm{syn}}}\right], \qquad \text{Eq. (11)}$$

where J^{+}_{syn} and J^{-}_{syn} are the upper and lower limits of the Gaussian distribution function and represent the maximum and minimum synaptic connection strengths. σ_{syn} is the standard deviation of the Gaussian distribution function and represents the synaptic connection width. $\Theta^{\mathrm{shift}}_{\mathrm{syn}}$ is the angular shift in the position of the set of cells targeted with the maximum connection strength relative to the position of the presynaptic cell. $\Theta^{\mathrm{shift}}_{\mathrm{syn}} = 0°$ for synapses where projections originate from E or I_{NEAR} cells, such that the Gaussian is centred at $\theta_i - \theta_j = 0°$. $\Theta^{\mathrm{shift}}_{\mathrm{syn}} = 180°$ for synapses where projections originate from I_{OPP} cells, such that the Gaussian is centred at $\theta_i - \theta_j = 180°$. J^{-}_{syn} is given by the normalisation of $W_{\mathrm{syn}}(\theta_i - \theta_j)$:

$$\frac{1}{360°} \int_{0°}^{360°} W_{\mathrm{syn}}(\theta_i - \theta_j) \mathrm{d}\theta_j = 1, \qquad \text{Eq. (12)}$$

such that:

$$J_{\mathrm{syn}}^{-} = \frac{360^\circ - \sqrt{2\pi\sigma_{\mathrm{syn}} J_{\mathrm{syn}}^{+}}}{360^\circ - \sqrt{2\pi\sigma_{\mathrm{syn}}}}. \qquad \text{Eq. (13)}$$

The J_{syn}^{+} and σ_{syn} parameters for each synaptic connection type are shown in Table 3.

D1R modulation: We modelled the effects of D1R occupancy on the NMDAR conductance at E→E synapses ($G_{\mathrm{E\to E,\ NMDA}}$), the AMPAR conductances at E→E and E→I synapses ($G_{\mathrm{E\to E,\ AMPA}}$ and $G_{\mathrm{E\to I,\ AMPA}}$), and the firing thresholds (V_{th}) of D1R+ I cells in the respective networks, as illustrated in Figure 4C. Notably, studying any other more complex D1R expression patterns within the different cell types was prohibited by the combinatorial explosion of possible patterns. Table 4 shows the NMDAR, AMPAR, and $GABA_A$R conductances and the decreases in the V_{th} of D1R+ I cells across networks and species for each D1R occupancy level.

From no to low D1R occupancy, specifically at $x = 0.125$, $G_{\mathrm{E\to E,\ NMDA}}$ increased in a step-like manner by 40%, mediated by postsynaptic D1Rs[31, 32], to facilitate a transition from a transient to a persistent firing activity regime, while $G_{\mathrm{E\to E,\ AMPA}}$ and $G_{\mathrm{E\to I,\ AMPA}}$ decreased, also step-like, by 20%, which aimed to capture a reduction of glutamate release putatively mediated by presynaptic D1Rs[31, 33], to dampen noise inputs to E and I cells. For mid, high, and very high D1R occupancy, $G_{\mathrm{E\to E,\ NMDA}}$, $G_{\mathrm{E\to E,\ AMPA}}$, and $G_{\mathrm{E\to I,\ AMPA}}$ were unchanged. $G_{\mathrm{E\to I,\ NMDA}}$ was not modulated across D1R occupancy levels because D1Rs and NMDARs do not interact at E→I synapses in layer III of primate (macaque) dlPFC[33]. We adopted Compte *et al.*'s[34] inhibitory $GABA_A$R conductances, which were unchanged across D1R occupancy levels because D1R stimulation does not modify action-potential independent GABA release from the presynaptic axon terminals of fast-spiking, putative PV neurons in layer III of primate (macaque) dlPFC[35]. Instead, based on Kröner *et al.*'s[35] finding that a V_{th} decrease accompanies the increase in intrinsic excitability of these inhibitory neurons with D1R stimulation, we decreased the V_{th} of D1R+ I cells across D1R occupancy levels according to network- and species-specific, shifted, and scaled sigmoid functions:

$$S(x) = y_{\max} + \frac{y_{\min} - y_{\max}}{1 + \exp(k(x - x_0))} \qquad \text{Eq. (14)}$$

The D1R expression in PV neurons, measured by the MOC in the automated classification analysis, determined the midpoint parameters, x_0, of the sigmoid for each species. Specifically, we set $x_0 = 0.50$ for the macaque as the reference and $x_0 = 0.36$ for the marmoset (base case #1). However, since MOC-measured D1R expression may not directly translate to D1R stimulation, we further explored two additional cases for the marmoset. Case #2 is characterised by a medium midpoint shift of 0.375 to $x_0 = 0.125$, while case #3 – by an extreme midpoint shift of 0.50 to $x_0 = 0$. Notably, leftward shifts smaller than the base case would have resulted in smaller-to-no differences in distractor resistance at the typical, mid D1R occupancy and hence were not explored. Heuristically, we choose a slope $k = -7$ to differentiate the idealised effects of the I cell thresholds on persistent activity for the five D1R occupancy levels. x represents the normalised range of D1R occupancy from 0 to 1. Crucially, the same D1R occupancy signifies a greater total number of DA-bound D1Rs, and thus greater D1R modulation, in the marmoset

compared to the macaque. Thresholds decreased for D1R+ I_{NEAR} cells in Network 1, D1R+ I_{OPP} cells in Network 2, and both D1R+ I cell types in Network 3 (Figure 4C2).

To identify the reasonable parameter sets that reproduce the inverted-U response for the macaque, we first conducted grid searches over (1) $G_{E\rightarrow E,\ NMDA}$, (2) $G_{E\rightarrow E,\ AMPA}$ and $G_{E\rightarrow I,\ AMPA}$, and (3) V_{th} for the D1R+ (i) I_{NEAR}, (ii) I_{OPP}, and (iii) I_{NEAR} and I_{OPP} cell types in, respectively, Networks 1, 2, and 3. For comparability, the $G_{E\rightarrow E,\ NMDA}$ for no D1R occupancy was approximately the highest $G_{E\rightarrow E,\ NMDA}$ not supporting persistent activity in any network. Also, we chose the minimum threshold ($V_{th,\min}$) for each network to fall approximately just beyond the bifurcation point up to which persistent activity could reliably form during the delay period. Notably, we selected the V_{th} at mid D1R occupancy ($x_0 = 0.50$) for each network to be the centre of the V_{th} parameter space for the spatially precise, noise- and distractor-resistant persistent activity regime, based on our assumption that this is the typical D1R stimulation level at which macaques function optimally under normal conditions. The baseline threshold ($V_{th,\text{base}}$) was the value located at an equal parameter distance from the V_{th} at mid D1R occupancy, as compared to the distance between the latter and $V_{th,\min}$ due to the symmetry of the sigmoid around the midpoint. Thus, interestingly, $V_{th,\text{base}}$ was -49.55 mV across networks. Then, to fit the V_{th} sigmoid ($x_0 = 0.50$, $k = -7$) for each network to the values identified in the grid searches, we estimated the upper and lower asymptotic limits, $y_{\max}$ and $y_{\min}$, to ensure that at $x = 0$, $V_{th,\text{base}} = -49.55$ mV and at $x = 1$, $V_{th,\min}$ equalled a value that was different across networks (Table 4). The respective $y_{\max}$ and $y_{\min}$ are given in Table 5. Overall, for macaque, in Network 1, I_{NEAR} thresholds decreased from $V_{th,\text{base}}$ for no D1R occupancy until a $V_{th,\min}$ of –52.05 mV for very high D1R occupancy. In Network 2, $V_{th,\min}$ was -52.30 mV because the model sustained persistent activity over a larger V_{th} range than Network 1. In Network 3, $V_{th,\min}$ was –51.50 mV because the higher net inhibition, due to decreasing the V_{th} of twice as many I cells (512, vs. 256 in Networks 1 and 2), shortens the V_{th} range that supports persistent activity. Consequently, the extent of V_{th} decreases across D1R occupancy levels in Network 3 was smaller than in Network 1, which in turn was smaller than in Network 2. Finally, we shifted the midpoint for Network 1's V_{th} sigmoid for the three marmoset cases, while keeping all other parameters the same.

We also fitted the D1R modulations of $G_{E\rightarrow E,\ AMPA}$ and $G_{E\rightarrow I,\ AMPA}$, together with the other D1R effects, to further neurophysiologically constrain network dynamics. Notably, presynaptic D1R-mediated reduction of fast non-NMDAR-mediated excitatory postsynaptic currents (EPSCs) (typically simulated by reducing G_{AMPA} in conductance-based models like ours) has been shown for E→I synapses in macaque layer III dlPFC[33]. However, to our knowledge, a similar explicit effect has not been reported for E→E synapses in primate layer III dlPFC. Furthermore, species, region, and layer differences in the D1R modulation of non-NMDAR-mediated EPSCs appear prevalent at E-E synapses (see Table 1 in the following works[36, 37]), in contrast to the well-established D1R-mediated increase in NMDAR-mediated EPSCs. The most relevant study on this issue showed a reduction in AMPAR-mediated EPSCs in macaque layer III dlPFC[38], but that effect was mediated by D1R and D2R co-activation and seemed to be specific to E→E synapses where the excitatory projection was long-range, with origins outside the microcircuit. Hence, we modelled the reduction in $G_{E\rightarrow I,\ AMPA}$ based on data from rat layer V mPFC instead[31]. Nevertheless, a computational study[39] showed that neither decreases nor increases of both $G_{E\rightarrow E,\ AMPA}$ and $G_{E\rightarrow I,\ AMPA}$ (concurrently) significantly or qualitatively changed the inverted-U relationship between working memory precision (i.e., the spatial tuning of the population activity of excitatory Delay cells) and D1R stimulation, possibly because AMPARs contribute little to persistent activity[25, 40] (but see[41]). Thus, ultimately, any different direction of the D1R effect on $G_{E\rightarrow E,\ AMPA}$ and/or $G_{E\rightarrow I,\ AMPA}$ should not change our conclusions.

Simulation protocol: We simulated five-second trials of a visuospatial working memory task mimicking Funahashi *et al.*'s protocol[42], but without an explicit response period. For a given trial, at a time point of T_{targ} = 400 ms, for a duration of Δt = 250 ms, we applied a target stimulus as a current injection of strength μ = 0.2* nA or 0.25** nA onto each E cell within an arc with a width of σ = 30° centred at an angle of Θ_{targ} = 0° on the ring. A 2050-ms target delay period followed. To test the distractor resistance of the microcircuit, we then presented a distractor stimulus at T_{dist} = 2700 ms, which was always of the same strength, width, and duration as the target stimulus but centred at Θ_{dist} = 180° (in Figure 5 and for the analysis of the inverted-U response across stimulus strengths in Figure S4 because at this position studies[34, 43] suggest distractor resistance would be most reliable under optimal conditions, maximizing our chances of capturing the peak of the inverted-U) or another position (for the analysis of the inverted-U response across distractor positions in Figure S5). The distractor delay period was also 2050 ms until the end of the trial. Thus, for a given I cell i, $I_{i,stim} = 0$, $stim \in \{targ, dist\}$, throughout trials, while for a given E cell i:

$$I_{i,stim}(t) = \begin{cases} \mu & \text{if } T_{stim} \leq t < T_{stim} + \Delta t, |\theta_i - \Theta_{stim}| \leq \frac{\sigma}{2} \\ 0 & \text{otherwise} \end{cases} \quad \text{Eq. (15)}$$

*Based on the analysis of the inverted-U response across stimulus strengths for Networks 1 and 2 in Figure S4; used in Figure 5 and for the analysis of the inverted-U response across distractor positions for Networks 1 and 2 in Figure S5.

**Based on the analysis of the inverted-U response across stimulus strengths for Network 3 in Figure S4, used for analysis of the inverted-U response across distractor positions for Network 3 in Figure S5, and for the I_{NEAR}-only and I_{OPP}-only networks in Figure S6.

Classification protocol: To classify the relevant dynamical regimes of the networks, representing stages of the inverted-U, as outcomes of task trials, we estimated the population vector[44, 45] from the activity of the E cell population during three periods: (1) baseline, from 0.2 to 0.4 secs of a trial (i.e. following the initial 0.2 secs after trial onset, to allow activity to equilibrate into a steady state, and until target stimulus presentation), (2) target delay, from 2.2 to 2.7 secs (i.e., until distractor stimulus presentation), and (3) distractor delay, from 4.5 to 5.0 secs (i.e., until the end of the trial). Thus, if [n_i, i = 1 ... 2048] are the spike counts of all E cells, labelled by an angle [θ_i, i = 1 ... 2048], during the respective trial period, the population vector is the normalized sum of each cell's selectivity vector, $e^{\mathbf{i}\theta_i}$, weighted by its spike count: $P = \left(\Sigma n_i e^{\mathbf{i}\theta_i}\right)(\Sigma n_i)^{-1}$, where the **i** in the exponential function is the imaginary unit. We extracted the population vector angle θ_{act} and modulus C: $P = Ce^{i\theta_{\text{act}}}$. For each trial period, we took θ_{act} as the decoded angle. Given that C quantifies the signal-to-noise ratio, we took it as a measure of confidence in the decoded angle. Like Cano-Colino *et al.*[46], we arbitrarily took a threshold of $C > 0.5$ as a criterion for confident decoding of θ_{act}.

We classified four dynamical regimes characterized by (1) transient activity, (2) noise- and distractor-resistant persistent activity, (3) distractible persistent activity, and (4) erroneous activity using the population vector angle θ_{act} and modulus C. In the transient activity regime, the confidence of the decoded θ_{act} during either or both the target and the distractor delay period was low ($C < 0.5$). Confident decoding of θ_{act} in only one of the delay periods also indicated a transient activity regime. Notably, we ensured that

the transient activity regime included only trials where the mean firing activity of active cells (i.e. that spiked at least once) during each period was ≤10 Hz. In the noise- and distractor-resistant persistent activity regime, we confidently decoded θ_{act} during both the target and distractor delay periods within +/-22.5° of the target position (0°). Notably, we excluded potential trials in which we may have confidently decoded θ_{act} within +/-22.5° of the target position during the baseline period (i.e. noise-evoked activity) due to uncertainty about whether any subsequent confident decoding of θ_{act} at the target position during the target and distractor delay periods is driven by the target stimulus or the noise-evoked activity. In the distractible persistent activity regime, we confidently decoded θ_{act} within +/-22.5° of the target position during the target delay period, but then also within +/-22.5° of the distractor position during the distractor delay period. Again, we excluded potential trials where we may have confidently decoded θ_{act} within +/-22.5° of the target position during the baseline period. The erroneous persistent activity regime accounted for any activity pattern that did not meet the conditions for the prior three regimes. For example, due to the overexcitation, at sub-optimal D1R occupancies in Networks 1-3, errors mainly involved noise-evoked or spatially diffuse persistent activity, reflected in confidently decoded θ_{act} at non-target positions (> +/-22.5° of the target). Conversely, due to the overinhibition, at supra-optimal D1R occupancies in Networks 1-3, errors mainly involved stimulus-evoked persistent activity but only for the target or for the distractor, reflected in confidently decoded θ_{act} at one but not both stimulus-specific positions (< +/-22.5°) during the respective period.

Analyses: For the analysis of the inverted-U response across stimulus strengths (Figure S4), we simulated 1000 trials for each unique parameter set, specifically for each network configuration (3), D1R occupancy level (5), and stimulus strength (17, from 0 to 0.40 pA, in steps of 0.025). We applied the classification protocol to all trials and then grouped them into 1000 sets, each containing one trial from each of the five D1R levels. For each network configuration, we then calculated the fraction of trial sets at each stimulus strength, in which the network reproduced the inverted-U response defined as (1) transient activity at no D1R occupancy, (2) any one of erroneous, noise- and distractor-resistant, or distractible persistent activity at low D1R occupancy, (3) noise- and distractor-resistant persistent activity at mid D1R occupancy, (4) distractible persistent activity at high D1R occupancy, and (5) transient activity at very high D1R occupancy.

For the analysis of the inverted-U response across distractor positions (Figure S5), we also simulated 1000 trials for each unique parameter set, specifically for each network configuration (3), D1R occupancy level (5), and distractor position (7, from 45.0° to 180.0° in steps of 22.5°). Again, we applied the classification protocol to all trials. Additionally, we conducted the same analysis and classification on two alternative networks (Figure S6), which comprised only, respectively, I_{NEAR} or I_{OPP} cells, in addition to the E cells. In these alternative networks, we maintained the total number of 512 I cells to match the net inhibitory drive across the I_{NEAR}-only and I_{OPP}-only networks for comparison with Network 3. Moreover, since, necessarily, all I cells in each alterative model expressed D1Rs because reproducing the inverted-U response requires dopaminergic modulation of inhibition, we used the D1R modulation parameters from Network 3. To reiterate, studying any other more complex D1R expression patterns, here specifically within the I cell types, was prohibited by the combinatorial explosion of possible patterns.

For the granulated analysis of the effect of the species difference in D1R expression on working memory performance in Network 1 (Figure S7), we again simulated 1000 trials for each unique parameter set. This included one case for the macaque and three cases for the marmoset, across 21 levels of D1R occupancy (from 0 to 1, in steps of 0.05). Once again, we applied the classification protocol to all trials.

Notably, within each analysis, the seed that generated the noise was different for each trial, serving to avoid bias and simulate the natural variability inherent in biological systems. Specifically, we utilized the simulation ID number as the seed (see Python script), thereby also ensuring reproducibility.

Numerical integration: We used a second-order Runge-Kutta integration algorithm with a time step of $\Delta t = 0.1$ ms for each simulation, which reportedly provided an optimal trade-off between computational tractability and precision in a similar spiking neural network[47].

Code availability: The custom script for the model was written in Python 3.10 using the Brian2 (Version 2.5.1) neural simulator[48] and will be made openly available on GitHub after publication. Simulations that ran on the high-performance computing facilities used Python 3.7 or 3.11.

Table 1.
Parameters of E and I cells.

Parameter	E cells	I cells
C_m	0.5 nF	0.2 nF
g_L	25 nS	20 nS
E_L	–70 mV	–70 mV
V_{th}	–50 mV	–50 mV ($V_{th,\mathrm{base}}$)
V_{res}	–60 mV	–60 mV
τ_{ref}	2 ms	1 ms

Table 2.
Parameters of NMDAR, AMPAR, and GABA$_A$R dynamics.

Receptor	V	τ	[Mg^{2+}]	τ_x	α_s
NMDAR	0 mV	100 ms	1 mM	2 ms	500 Hz
AMPAR	0 mV	2 ms			
GABA$_A$R	70 mV	10 ms			

Table 3.
Widths (adopted from Cano-Colino et al.[46]) and maximum strengths of each synaptic connection type.

Synaptic Connection Type	σ	J^+
E→E	14.4°	2.1
E→I	14.4°	1.6
I→E	14.4°	1.6
I→I	14.4°	2.1

Table 4.
Synapse-specific receptor conductances and I cell firing thresholds for each network, species, and D1R occupancy. Colour-coding is according to the D1R modulations represented in Figure 4C2.

Parameter	Network	Species	NO D1R	LOW D1R	MID D1R	HIGH D1R	VERY HIGH D1R
$G_{E\to E,\ NMDA}$ (nS)	1-3	MAC & MARM	0.220	0.308	0.308	0.308	0.308
$G_{E\to I,\ NMDA}$	1-3	MAC & MARM	0.212	0.212	0.212	0.212	0.212
$G_{E\to E,\ AMPA}$	1-3	MAC & MARM	0.284	0.226	0.226	0.226	0.226
$G_{E\to I,\ AMPA}$	1-3	MAC & MARM	0.217	0.173	0.173	0.173	0.173
$g_{ext\to E,\ AMPA}$	1-3	MAC & MARM	3.1	3.1	3.1	3.1	3.1
$g_{ext\to I,\ AMPA}$	1-3	MAC & MARM	2.38	2.38	2.38	2.38	2.38
$G_{I\to E,\ GABA_A}$	1-3	MAC & MARM	1.336	1.336	1.336	1.336	1.336
$G_{I\to I,\ GABA_A}$	1-3	MAC & MARM	1.024	1.024	1.024	1.024	1.024
V_{th} [I_{NEAR}] (mV)	1	MAC	-49.55	-49.86	-50.80	-51.74	-52.05
V_{th} [I_{OPP}]	2	MAC	-49.55	-49.90	-50.93	-51.95	-52.30
V_{th} [I_{NEAR}, I_{OPP}]	3	MAC	-49.55	-49.80	-50.53	-51.26	-51.51
V_{th} [I_{NEAR}]	I_{NEAR}-only	MAC	-49.55	-49.80	-50.53	-51.26	-51.51
V_{th} [I_{OPP}]	I_{OPP}-only	MAC	-49.55	-49.80	-50.53	-51.26	-51.51
V_{th} [I_{NEAR}]	1	MARM (BASE)	-49.67	-50.31	-51.40	-51.97	-52.10
V_{th} [I_{NEAR}]	1	MARM (MEDIUM)	-50.25	-51.35	-51.95	-52.10	-52.12
V_{th} [I_{NEAR}]	1	MARM (EXTREME)	-50.80	-51.74	-52.05	-52.12	-52.13

Table 5.
Upper and lower asymptotic limits, y_{max} and y_{min}, of the sigmoid functions for each network.

Network	1	2	3	I_{NEAR}-only	I_{OPP}-only
y_{max}	−49.47	−49.46	−49.49	−49.49	−49.49
y_{min}	−52.13	−52.39	−51.57	−51.57	−51.57

References

1. Mitchell, J.F., Reynolds, J.H. & Miller, C.T. Active Vision in Marmosets: A Model System for Visual Neuroscience. *The Journal of Neuroscience* **34**, 1183-1194 (2014).
2. Nandy, A.S., Sharpee, T.O., Reynolds, J.H. & Mitchell, J.F. The fine structure of shape tuning in area V4. *Neuron* **78**, 1102-1115 (2013).
3. Krienen, F.M.*, et al.* A marmoset brain cell census reveals regional specialization of cellular identities. *Sci Adv* **9**, eadk3986 (2023).
4. Datta, D.*, et al.* Key Roles of CACNA1C/Cav1.2 and CALB1/Calbindin in Prefrontal Neurons Altered in Cognitive Disorders. *JAMA Psychiatry* (2024).
5. Krienen, F.M.*, et al.* A marmoset brain cell census reveals persistent influence of developmental origin on neurons. *bioRxiv*, 2022.2010.2018.512442 (2022).
6. Saunders, A.*, et al.* Molecular Diversity and Specializations among the Cells of the Adult Mouse Brain. *Cell* **174**, 1015-1030.e1016 (2018).
7. Krienen, F.M.*, et al.* Innovations present in the primate interneuron repertoire. *Nature* **586**, 262-269 (2020).
8. Ma, S.*, et al.* Molecular and cellular evolution of the primate dorsolateral prefrontal cortex. *Science*, eabo7257 (2022).
9. Yao, Z.*, et al.* A taxonomy of transcriptomic cell types across the isocortex and hippocampal formation. *Cell* **184**, 3222-3241 e3226 (2021).
10. Squair, J.W.*, et al.* Confronting false discoveries in single-cell differential expression. *Nature communications* **12**, 5692 (2021).
11. Schilder BM Skene NG. orthogene: an R package for easy mapping of orthologous genes across hundreds of species. (Bioconductor, 2022).
12. Robinson, M.D., McCarthy, D.J. & Smyth, G.K. edgeR: a Bioconductor package for differential expression analysis of digital gene expression data. *Bioinformatics* **26**, 139-140 (2009).
13. Wong, R.K., Selvanayagam, J., Johnston, K.D. & Everling, S. Delay-related activity in marmoset prefrontal cortex. *Cereb Cortex* **33**, 3523-3537 (2023).
14. Stojanovic, T.*, et al.* Validation of dopamine receptor DRD1 and DRD2 antibodies using receptor deficient mice. *Amino Acids* **49**, 1101-1109 (2017).
15. Glausier, J.R., Khan, Z.U. & Muly, E.C. Dopamine D1 and D5 receptors are localized to discrete populations of interneurons in primate prefrontal cortex. *Cereb Cortex* **19**, 1820-1834 (2009).
16. Paspalas, C.D. & Goldman-Rakic, P.S. Microdomains for dopamine volume neurotransmission in primate prefrontal cortex. *J Neurosci* **24**, 5292-5300 (2004).
17. Paspalas, C.D. & Goldman-Rakic, P.S. Presynaptic D1 dopamine receptors in primate prefrontal cortex: target-specific expression in the glutamatergic synapse. *J Neurosci* **25**, 1260-1267 (2005).
18. Mueller, A., Krock, R.M., Shepard, S. & Moore, T. Dopamine Receptor Expression Among Local and Visual Cortex-Projecting Frontal Eye Field Neurons. *Cereb Cortex* **30**, 148-164 (2020).
19. Joyce, M.K.P., Garcia-Cabezas, M.A., John, Y.J. & Barbas, H. Serial Prefrontal Pathways Are Positioned to Balance Cognition and Emotion in Primates. *J Neurosci* **40**, 8306-8328 (2020).
20. Schindelin, J.*, et al.* Fiji: an open-source platform for biological-image analysis. *Nature methods* **9**, 676-682 (2012).
21. Stauffer, W., Sheng, H. & Lim, H.N. EzColocalization: An ImageJ plugin for visualizing and measuring colocalization in cells and organisms. *Scientific reports* **8**, 15764 (2018).
22. Tsolias, A. & Medalla, M. Muscarinic Acetylcholine Receptor Localization on Distinct Excitatory and Inhibitory Neurons Within the ACC and LPFC of the Rhesus Monkey. *Front Neural Circuits* **15**, 795325 (2021).

23. Tuckwell, H.C. *Introduction to theoretical neurobiology* (Cambridge University Press, New York, N.Y., U.S.A., 1988).
24. Troyer, T.W. & Miller, K.D. Physiological gain leads to high ISI variability in a simple model of a cortical regular spiking cell. *Neural Comput* **9**, 971-983 (1997).
25. Wang, X.J. Synaptic basis of cortical persistent activity: the importance of NMDA receptors to working memory. *J Neurosci* **19**, 9587-9603 (1999).
26. Jahr, C.E. & Stevens, C.F. Voltage dependence of NMDA-activated macroscopic conductances predicted by single-channel kinetics. *J Neurosci* **10**, 3178-3182 (1990).
27. Hestrin, S., Sah, P. & Nicoll, R.A. Mechanisms generating the time course of dual component excitatory synaptic currents recorded in hippocampal slices. *Neuron* **5**, 247-253 (1990).
28. Spruston, N., Jonas, P. & Sakmann, B. Dendritic glutamate receptor channels in rat hippocampal CA3 and CA1 pyramidal neurons. *J Physiol* **482 (Pt 2)**, 325-352 (1995).
29. Salin, P.A. & Prince, D.A. Spontaneous GABAA receptor-mediated inhibitory currents in adult rat somatosensory cortex. *J Neurophysiol* **75**, 1573-1588 (1996).
30. Xiang, Z., Huguenard, J.R. & Prince, D.A. GABAA receptor-mediated currents in interneurons and pyramidal cells of rat visual cortex. *J Physiol* **506 (Pt 3)**, 715-730 (1998).
31. Seamans, J.K., Durstewitz, D., Christie, B.R., Stevens, C.F. & Sejnowski, T.J. Dopamine D1/D5 receptor modulation of excitatory synaptic inputs to layer V prefrontal cortex neurons. *Proc Natl Acad Sci USA* **98**, 301-306 (2001).
32. Durstewitz, D., Seamans, J.K. & Sejnowski, T.J. Dopamine-mediated stabilization of delay-period activity in a network model of prefrontal cortex. *J Neurophysiol* **83**, 1733-1750 (2000).
33. Gonzalez-Burgos, G., Kroener, S., Seamans, J.K., Lewis, D.A. & Barrionuevo, G. Dopaminergic modulation of short-term synaptic plasticity in fast-spiking interneurons of primate dorsolateral prefrontal cortex. *J Neurophysiol.* **94**, 4168-4177 (2005).
34. Compte, A., Brunel, N., Goldman-Rakic, P.S. & Wang, X.J. Synaptic mechanisms and network dynamics underlying spatial working memory in a cortical network model. *Cereb Cortex* **10**, 910-923 (2000).
35. Kröner, S., Krimer, L.S., Lewis, D.A. & Barrionuevo, G. Dopamine increases inhibition in the monkey dorsolateral prefrontal cortex through cell type-specific modulation of interneurons. *Cereb Cortex* **17**, 1020-1032 (2007).
36. Darvish-Ghane, S., Quintana, C., Beaulieu, J.M. & Martin, L.J. D1 receptors in the anterior cingulate cortex modulate basal mechanical sensitivity threshold and glutamatergic synaptic transmission. *Mol Brain* **13**, 121 (2020).
37. Darvish-Ghane, S. Dopaminergic Modulation of Ionotropic Transmission in the Anterior Cingulate Cortex in Naïve and Inflammatory Pain States. (Doctoral Dissertation, University of Toronto, 2022).
38. Urban, N.N., Gonzalez-Burgos, G., Henze, D.A., Lewis, D.A. & Barrionuevo, G. Selective reduction by dopamine of excitatory synaptic inputs to pyramidal neurons in primate prefrontal cortex. *J Physiol* **539**, 707-712 (2002).
39. Okimura, T., Tanaka, S., Maeda, T., Kato, M. & Mimura, M. Simulation of the capacity and precision of working memory in the hypodopaminergic state: Relevance to schizophrenia. *Neuroscience* **295**, 80-89 (2015).
40. Wang, M.*, et al.* NMDA receptors subserve persistent neuronal firing during working memory in dorsolateral prefrontal cortex. *Neuron* **77**, 736-749 (2013).
41. van Vugt, B., van Kerkoerle, T., Vartak, D. & Roelfsema, P.R. The Contribution of AMPA and NMDA Receptors to Persistent Firing in the Dorsolateral Prefrontal Cortex in Working Memory. *J Neurosci* **40**, 2458-2470 (2020).

42. Funahashi, S., Bruce, C.J. & Goldman-Rakic, P.S. Mnemonic coding of visual space in the monkey's dorsolateral prefrontal cortex. *J Neurophysiol* **61**, 331-349 (1989).
43. Suzuki, M. & Gottlieb, J. Distinct neural mechanisms of distractor suppression in the frontal and parietal lobe. *Nat Neurosci* **16**, 98-104 (2013).
44. Georgopoulos, A.P., Schwartz, A.P. & Kettner, R.E. Neuronal population coding of movement direction. *Science* **233**, 1416-1419 (1986).
45. Lee, C., Rohrer, W.H. & Sparks, D.L. Population coding of saccadic eye movements by neurons in the superior colliculus. *Nature* **332**, 357-360 (1988).
46. Cano-Colino, M., Almeida, R., Gomez-Cabrero, D., Artigas, F. & Compte, A. Serotonin regulates performance nonmonotonically in a spatial working memory network. *Cereb Cortex* **24**, 2449-2463 (2014).
47. Ramirez-Mahaluf, J.P., Roxin, A., Mayberg, H.S. & Compte, A. A Computational Model of Major Depression: the Role of Glutamate Dysfunction on Cingulo-Frontal Network Dynamics. *Cereb Cortex* **27**, 660-679 (2017).
48. Stimberg, M., Brette, R. & Goodman, D.F. Brian 2, an intuitive and efficient neural simulator. *eLife* **8** (2019).